Ca hnk: The Calcium-rich Transient Supernova 2016hnk from a Helium Shell Detonation of a Sub-Chandrasekhar White Dwarf

Wynn V. Jacobson-Galán[1,2,3] , Abigail Polin[4,5,6], Ryan J. Foley[3], Georgios Dimitriadis[3] , Charles D. Kilpatrick[3] ,
Raffaella Margutti[1,2] , David A. Coulter[3] , Saurabh W. Jha[7] , David O. Jones[3] , Robert P. Kirshner[8], Yen-Chen Pan[9,13] ,
Anthony L. Piro[10] , Armin Rest[11,12], and César Rojas-Bravo[3]

[1] Department of Physics and Astronomy, Northwestern University, 2145 Sheridan Road, Evanston, IL 60208, USA; wynn@u.northwestern.edu
[2] Center for Interdisciplinary Exploration and Research in Astrophysics (CIERA), 1800 Sherman Avenue, Evanston, IL 60201, USA
[3] Department of Astronomy and Astrophysics, University of California, Santa Cruz, CA 95064, USA
[4] Department of Physics, University of California, Berkeley, CA 94720, USA
[5] Department of Astronomy, University of California, Berkeley, CA 94720, USA
[6] Lawrence Berkeley National Laboratory, Berkeley, CA 94720, USA
[7] Department of Physics and Astronomy, Rutgers, the State University of New Jersey, 136 Frelinghuysen Road, Piscataway, NJ 08854, USA
[8] Harvard College Observatory, 60 Garden Street, Cambridge, MA 02138, USA
[9] Division of Science, National Astronomical Observatory of Japan, 2-21-1 Osawa, Mitaka, Tokyo 181-8588, Japan
[10] The Observatories of the Carnegie Institution for Science, 813 Santa Barbara Street, Pasadena, CA 91101, USA
[11] Space Telescope Science Institute, Baltimore, MD 21218, USA
[12] Department of Physics and Astronomy, The Johns Hopkins University, Baltimore, MD 21218, USA

Abstract

We present observations and modeling of SN 2016hnk, a Ca-rich supernova (SN) that is consistent with being the result of a He-shell double-detonation explosion of a C/O white dwarf. We find that SN 2016hnk is intrinsically red relative to typical thermonuclear SNe and has a relatively low peak luminosity ($M_B = -15.4$ mag), setting it apart from low-luminosity SNe Ia. SN 2016hnk has a fast-rising light curve that is consistent with other Ca-rich transients ($t_r = 15$ days). We determine that SN 2016hnk produced $0.03 \pm 0.01\,M_\odot$ of ^{56}Ni and $0.9 \pm 0.3\,M_\odot$ of ejecta. The photospheric spectra show strong, high-velocity Ca II absorption and significant line blanketing at $\lambda < 5000$ Å, making it distinct from typical (SN 2005E-like) Ca-rich SNe. SN 2016hnk is remarkably similar to SN 2018byg, which was modeled as a He-shell double-detonation explosion. We demonstrate that the spectra and light curves of SN 2016hnk are well modeled by the detonation of a $0.02\,M_\odot$ helium shell on the surface of a $0.85\,M_\odot$ C/O white dwarf. This analysis highlights the second observed case of a He-shell double-detonation and suggests a specific thermonuclear explosion that is physically distinct from SNe that are defined simply by their low luminosities and strong [Ca II] emission.

1. Introduction

Type Ia supernovae (SNe Ia) are produced by the thermonuclear explosion of a C/O white dwarf (WD) in a binary system (Hoyle & Fowler 1960; Colgate & McKee 1969; Woosley et al. 1986). Due to their standardizable light-curve evolution, SNe Ia are used as cosmological probes of the universe's accelerating expansion (Riess et al. 1998; Perlmutter et al. 1999). However, there exists an amalgam of subluminous thermonuclear objects that deviate from typical SN Ia characteristics (see Taubenberger 2017 for a review). Such physically distinct classes of "WD SNe" include: 91bg-like (Filippenko et al. 1992), 02es-like (Ganeshalingam et al. 2012), "fast-decliners" (Kasliwal et al. 2010; Perets et al. 2011; Drout et al. 2013), 06bt-like (Foley et al. 2010), SNe Iax (Foley et al. 2013), and Ca-rich transients (Filippenko et al. 2003; Perets et al. 2010).

"Ca-rich" SNe are a particularly heterogeneous group of objects which, similar to other thermonuclear objects, are thought to arise from a progenitor system containing a WD. Ca-rich objects are primarily characterized by peak magnitudes of

−14 to −16.5, quickly evolving light curves, and strong calcium features in photospheric and nebular phase spectra (Taubenberger 2017). In nebular spectra, these objects show weak Fe line transitions, with [Ca II] $\lambda\lambda$7291, 7324 being the dominant emission feature. Ca-rich transients have detectable [O I] $\lambda\lambda$6300, 6364 emission in nebular spectra, but a defining feature of the class is an integrated [Ca II]/[O I] flux ratio greater than ∼2. Furthermore, the majority of these objects exhibit low ejecta and ^{56}Ni masses of $\lesssim 0.5\,M_\odot$ and $\lesssim 0.1\,M_\odot$, respectively (Perets et al. 2010; Lunnan et al. 2017; however, see Milisavljevic et al. 2017).

Significant variations in the physical characteristics of "Ca-rich" transients have resulted in a highly diverse class of objects. For example, there is a substantial spread in [Ca II]/[O I] flux ratios among Ca-rich transients: objects such as SN 2003dg, PTF09dav, and PTF10iuv have negligible [O I] emission, while SN 2012hn has a comparable oxygen composition to Type IIb/IIP SNe during the nebular phase (e.g., Valenti et al. 2014). Additionally, the presence of Hα emission in PTF09dav and iPTF15eqv is unlike anything observed within the Ca-rich class (Sullivan et al. 2011; Milisavljevic et al. 2017). The lack of helium in addition to the probable presence of Sc II, Cr II, and Sr II also makes

---

[13] EACOA Fellow.

PTF09dav an outlier within the class. Furthermore, the location of iPTF15eqv in a star-forming, late-type galaxy, plus its large inferred ejecta mass ($\approx$2–4 $M_\odot$), is difficult to reconcile with other homogeneous properties of Ca-rich transients (Milisavljevic et al. 2017). Lastly, many other thermonuclear objects have been discovered with strong Ca II absorption (e.g., SN 2018byg; De et al. 2019) and even SNe Iax can be considered "Ca-rich" based on their [Ca II]/[O I] flux ratios. However, despite the constraints given by the current sample of Ca-rich objects, a core-collapse SN origin cannot yet be fully ruled out given the diversity in physical characteristics and host environments within this class.

The significant fraction of objects found in old stellar environments on the outskirts of early-type galaxies supports a WD origin for at least some Ca-rich transients (Perets et al. 2011; Kasliwal et al. 2012). Parenthetically, Foley (2015) demonstrate that these SNe tend to be found in dense environments of merged/merging galaxies with a large range of observed velocity offsets that are anti-correlated with the projected offsets. This finding is also supported by Lunnan et al. (2017) who showed that Ca-rich transients were typically produced in group or cluster environments of early-type elliptical galaxies. Furthermore, non-detections of star-forming regions at Ca-rich transient explosion sites indicated that their progenitors were likely not formed at the SN location, i.e., in situ (Lyman et al. 2014).

A variety of progenitor scenarios involving the thermonuclear explosion of a WD have been proposed to explain the peculiar properties of Ca-rich transients and their environments. Accretion-induced collapse of a WD into a neutron star (NS) will produce a sub-luminous explosion. However, the combination of a very rapid rise time ($\sim$1 day), high expansion velocities, and over-production of intermediate-mass elements makes this an unlikely scenario (Metzger et al. 2009). Similar discrepancies between models and observations also rule out the tidal disruptions of WDs by NSs or stellar-mass black holes (BHs) (Metzger 2012; Margalit & Metzger 2016; Toonen et al. 2018; Zenati et al. 2019a, 2019b). Tidal detonations of a WD by interaction with an intermediate-mass BH (IMBH) do occur in dense stellar systems, but are difficult to reconcile due to the lack of observed IMBHs at the locations of Ca-rich transients (Rosswog et al. 2008; MacLeod et al. 2014; Sell et al. 2015).

Given the range of observed properties, a highly promising progenitor channel for peculiar thermonuclear SNe such as Ca-rich transients is the detonation of a helium-accreting WD. One such model involves the explosion of a sub-Chandrasekhar mass, C/O WD via an initial detonation of a surface layer of accreted helium (Nomoto 1982a, 1982b; Woosley et al. 1986; Woosley & Weaver 1994; Livne & Arnett 1995). Alternatively, thin helium shell detonations that only partially disrupt the core can result in rapidly evolving, low-luminosity explosions often labeled as .Ia SNe (Bildsten et al. 2007; Shen et al. 2010). However, the rise-times and ejecta masses produced in .Ia explosions are inconsistent with those of Ca-rich objects.

A helium shell detonation scenario has been employed to model photometric and spectroscopic signatures in SNe Ia (Kromer et al. 2010; Sim et al. 2010; Woosley & Kasen 2011; Polin et al. 2019a; Townsley et al. 2019). While this model can reproduce the observational properties of normal SNe Ia, there exists a wide parameter space within the double-detonation scenario that can be used to explain atypical objects. Variations on the initial WD mass and chemical composition, as well as

helium shell mass, can explain the sub-luminous SNe Ia such as 91bg-like objects (Shen et al. 2018). Additionally, a helium shell detonation was invoked to explain the Ca-rich transient SN 2005E, which showed observational consistency to a low-mass WD detonation with a thick helium shell (Waldman et al. 2011).

Recently, observations of SN Ia 2018byg (ZTF18aaqeasu) were presented as the first evidence of a helium shell double detonation (De et al. 2019). SN 2018byg showed spectroscopic and photometric consistency with a 0.15 $M_\odot$ helium shell detonation on a 0.75 $M_\odot$, sub-Chandrasekhar mass WD in which material was mixed in the outer layers of ejecta. This specific thick-shell model was presented by Polin et al. (2019a) who showed that the parameter space of such an explosion scenario is well-matched to observations of SNe Ia. In Section 5, we present specific helium shell detonation models and discuss the viability of this explosion mechanism in explaining observations of SN 2016hnk.

In this paper we present observations, analysis, and modeling of the peculiar thermonuclear transient SN 2016hnk. Upon discovery, this object was originally classified as an SN Ia with photometric and spectroscopic similarities to both SN 1991bg and the Ca-rich transient PTF09dav. Sell et al. (2018) identified the object as a candidate Ca-rich gap transient and observed the SN with Chandra to test a progenitor scenario involving a tidal detonation of a WD by an IMBH. Finding no evidence of the predicted X-ray emission, Sell et al. were able to rule out this progenitor scenario. However, the observed X-ray detection limits cannot constrain a WD + NS (or stellar-mass BH) progenitor scenario. Galbany et al. (2019) (hereafter G19) present multi-wavelength observations of SN 2016hnk and conclude that this object belongs to the 91bg-like subclass. Through NLTE spectral modeling of SN 2016hnk, G19 argue for a progenitor scenario involving a low-luminosity detonation of a Chandrasekhar mass WD. We discuss these interpretations of SN 2016hnk throughout the paper as well as present alternative conclusions on the origin and classification of this intriguing object.

In Section 2, we present observations and data reduction of SN 2016hnk. In Section 3, we present photometric properties of SN 2016hnk and discuss how these measurements compare to different classes of transient objects. In Section 4, we present spectroscopic properties and spectral comparisons. In Section 5, we compare light curve and spectral models of helium shell detonations to SN 2016hnk. In Section 6, we discuss both the potential progenitor scenarios for SN 2016hnk and how our findings compare to those of G19.

2. Observations

2.1. Detection and Classification

SN 2016hnk was discovered by the Asteroid Terrestrial-impact Last Alert System (ATLAS; Tonry et al. 2018) on 2016 October 27 (MJD 57688) using the ACAM1 instrument with a cyan filter (Tonry et al. 2016). SN 2016hnk has a discovery apparent magnitude of 17.91 and is located at $\alpha = 02^{\rm h}13^{\rm m}16\overset{s}{.}63$, $\delta = -07°39'40\overset{''}{.}80$. SN 2016hnk is located $1\overset{''}{.}4$ east and $12\overset{''}{.}4$ north of the nucleus of the SBa galaxy MCG-01-06-070. In this paper, we use the reported host-galaxy distance and redshift of 72.9 Mpc and 0.016268, respectively, in standard ΛCDM cosmology ($H_0 = 70\,{\rm km\,s^{-1}\,Mpc^{-1}}$, $\Omega_M = 0.27$, $\Omega_\Lambda = 0.63$).
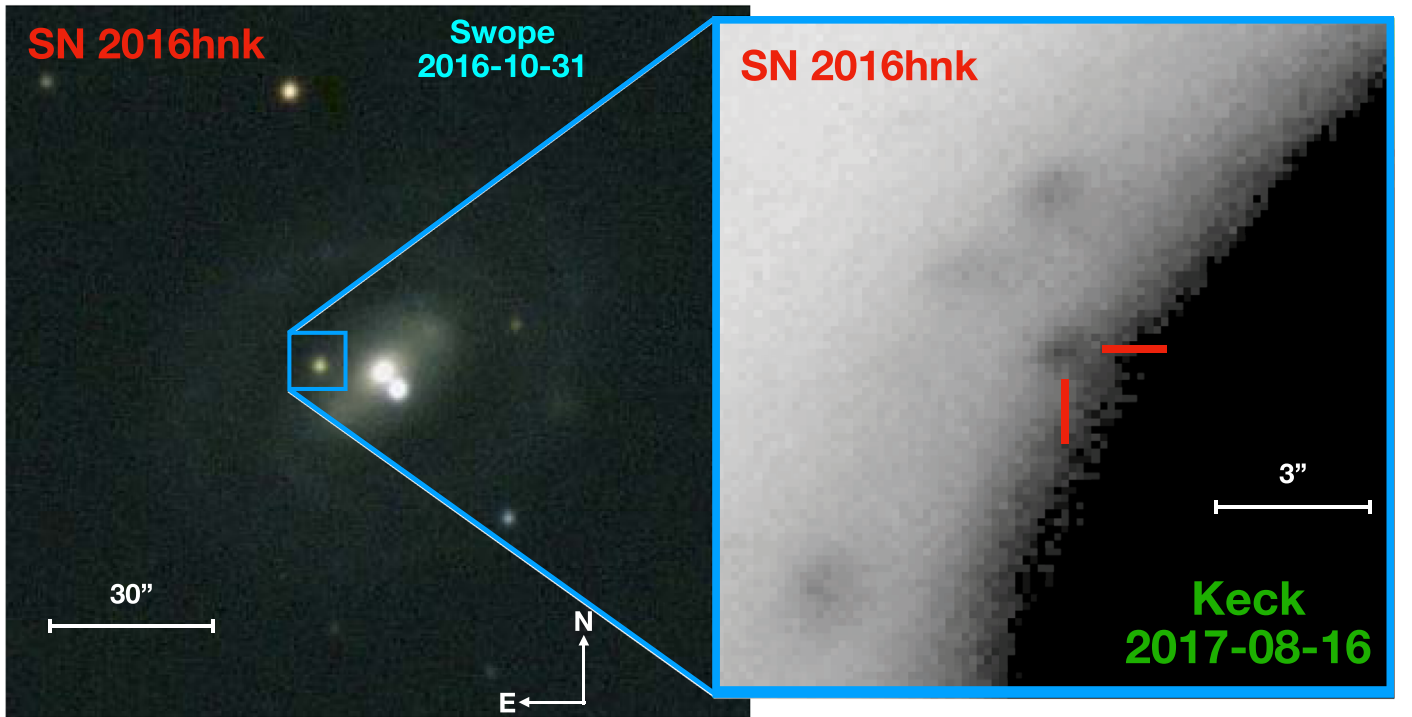
Figure 1. Left: RGB false-color image of SN 2016hnk taken by the Swope telescope two days after *B*-band maximum. RGB image generated using *r, V*, and *B*-bands. Right: *I*-band Keck Low-resolution Imaging Spectrometer image at +291 days. Source marked in red.

SN 2016hnk was first classified as a peculiar SN Ia by Cannizzaro et al. (2016) who noted its resemblance to SN 1991bg (91bg-like) near maximum light. The initial spectrum was described as being red, with the presence of strong Si II λ6355, O I λ7774, and near-infrared Ca II spectral features. Dimitriadis et al. (2016) made a similar classification and indicated the similarity of SN 2016hnk with SNe 1991bg and 1999by. Finally, the classification by Pan et al. (2016) illustrated a similarity between SN 2016hnk and the Ca-rich transient PTF09dav (Sullivan et al. 2011) given their similar colors, peak absolute magnitude, and spectral features. Pan et al. noted the distinct absorption profiles at 5350, 5540, and 7120 Å, which Sullivan et al. (2011) attributed to Sc II (first two) and Ti II (third). We discuss these specific spectral features in Section 4.2.

2.2. Early-time Photometry

We imaged SN 2016hnk between 2016 November 1 and 2017 February 17 with the Direct camera on the Swope 1 m telescope at Las Campanas Observatory, Chile. Observations were performed in Johnson *BV* and Sloan *ugri* filters. We performed bias-subtraction and flat-fielding, stitching, registration, and photometric calibration using photpipe (Rest et al. 2005). For our photometric calibration, we used stars in the Pan-STARRS PS1 DR1 catalog (Flewelling et al. 2016) transformed from *gri* magnitudes to the *uBVgri* Swope natural system following the Supercal method (Scolnic et al. 2015). Difference imaging was performed using Swope *BVgri* and *u* templates obtained on 2017 November 15 and 2017 December 10, respectively. Final photometry was performed in the difference images with DoPhot (Schechter et al. 1993). A Swope *Bri* image of SN 2016hnk, mapped to RGB channels, from 2016 October 31, is shown in Figure 1.

Additional imaging of SN 2016hnk was obtained by the Las Cumbres Observatory Global Telescope (LCOGT; Brown et al. 2013) and the Foundation Supernova Survey with Pan-STARRS (Foley et al. 2018). We performed a similar photometric reduction on the LCOGT data as the Swope imaging, which included standard subtractions and difference imaging. PS1 images of SN 2016hnk were reduced with the same custom-built pipeline as for the PS1 Medium Deep Field survey data. The basic data processing was performed by the PS1 Image Processing Pipeline (Magnier 2006; Magnier et al. 2013; Waters et al. 2016). Single-epoch images were then processed through a frame-subtraction analysis using phot-pipe, which determines an appropriate spatially varying convolution kernel using HOTPANTS (Becker 2015). After the convolutions were performed, the template image was subtracted from the survey image. Detections of significant flux excursions in the difference images were found using DoPHOT (Schechter et al. 1993).

SN 2016hnk has a reported Milky Way reddening and associated extinction of $E(B - V) = 0.0224$ mag and $A_V = 0.069$ mag (Schlegel et al. 1998; Schlafly & Finkbeiner 2011), respectively, which we correct for using a standard Fitzpatrick (1999) reddening law and $R_V = 3.1$. We do not correct for host-galaxy contamination given the absence of Na I D absorption in all spectra at the host redshift. We demonstrate the effect of further de-reddening in the color curves shown in Figure 7 and discuss the intrinsic color of SN 2016hnk in Section 6.1.

Galbany et al. (2019) report a host extinction of $E(B - V) = 0.45$ mag using the observed ratio of Hα and Hβ fluxes from host-galaxy spectra. However, because the exact vertical location of the source in the galaxy is unknown, Na I D absorption is the most accurate indicator of extinction at the site of the explosion. Thus all multi-color optical photometry of SN 2016hnk in Figure 2 has only been corrected for Milky
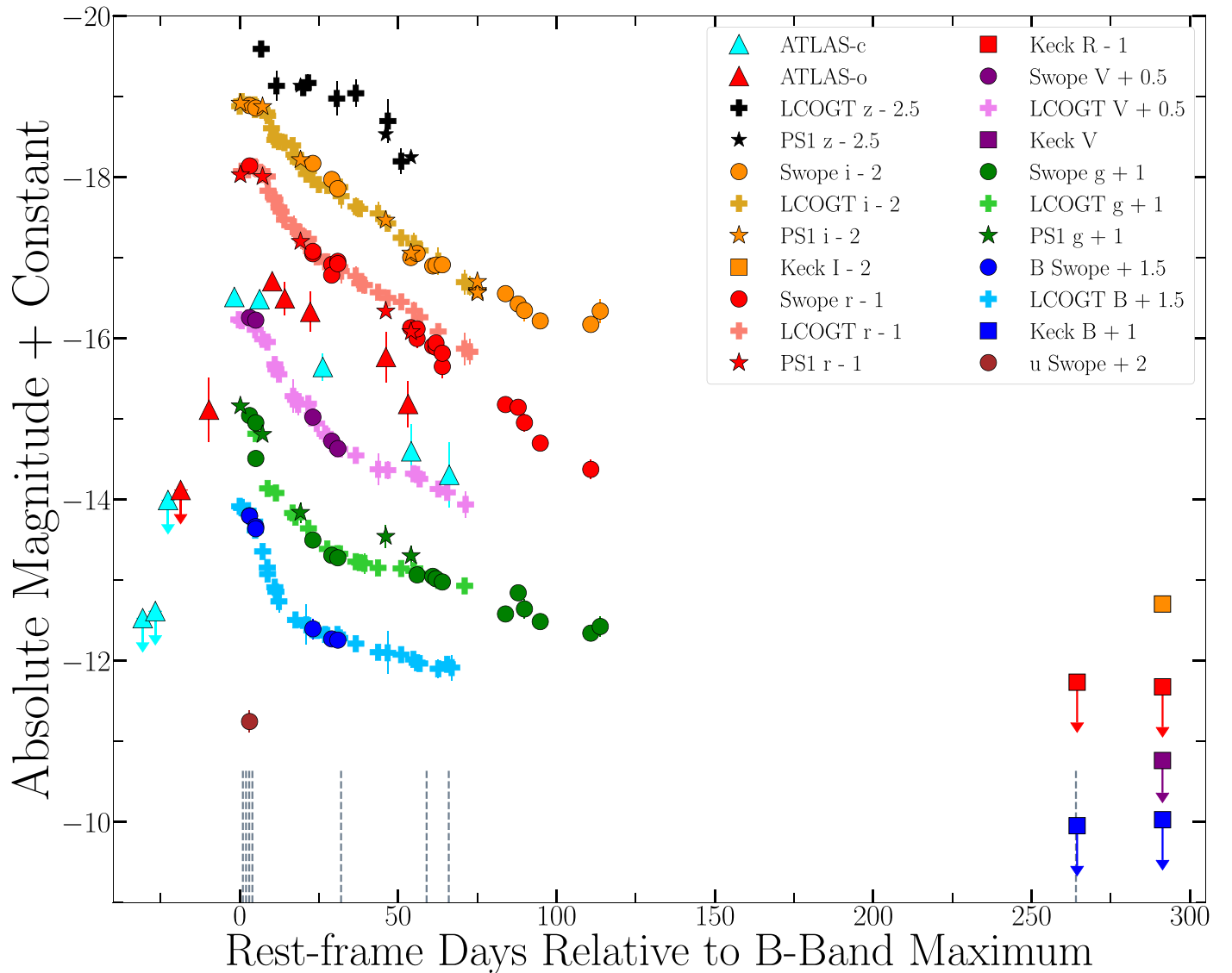
Figure 2. Optical light curve of SN 2016hnk with respect to *B*-band maximum. ATLAS data presented as triangles, Pan-STARRS as stars, Swope as circles, LCOGT as plus signs, and Keck as squares. All Keck Low-resolution Imaging Spectrometer data points are non-detections with the exception of the *I*-band point at +291 days shown in orange. The epochs of our spectral observations are marked by gray dashed lines.

Way extinction. All photometric observations are listed in Table A1.

2.3. Late-time Keck Imaging

Final photometric observations of SN 2016hnk were obtained using the imaging camera on the Keck telescope Low-resolution Imaging Spectrometer (LRIS; Oke et al. 1995). The source was observed on 2017 July 20 in *BR* as well as on 2017 August 16 in *BVRI*. Observations were performed in the blue and red channels simultaneously with the *B+R* filters and *V+I* filters and the D560 dichroic, and reduced using `photpipe`. For our photometric calibration, we used secondary calibrators in each image with magnitudes derived from SDSS standard stars transformed to the *BVRI* system (Bilir et al. 2011; Alam et al. 2015). Keck *BVRI* templates were acquired on 2019 September 25 and image subtraction was performed using `HOTPANTS`. Final photometry was performed on the difference images using `photpipe`. The only late-time

detection of SN 2016hnk was in the *I*-band at a phase of +291 days relative to maximum light. The *I*-band detection image is shown in Figure 1 and has an associated apparent magnitude of 23.57 ± 0.09 mag.

All recovered magnitudes in other Keck filters are reported as upper limits as shown in the full optical light curve in Figure 2 and listed in Table A1.

2.4. Optical Spectroscopy

In Figure 3, we present optical spectral observations of SN 2016hnk from +1 to +264 days relative to *B*-band maximum. We first observed SN 2016hnk on 2016 October 30 with the Goodman High Throughput Spectrograph (Clemens et al. 2004) on the Southern Astrophysical Research Telescope (SOAR). SN 2016hnk was then observed using the Kitt Peak Ohio State Multi-object Spectrograph (KOSMOS; Martini et al. 2014) on 2016 November 30 and December 27 as well as with SOAR on 2017 January 3.
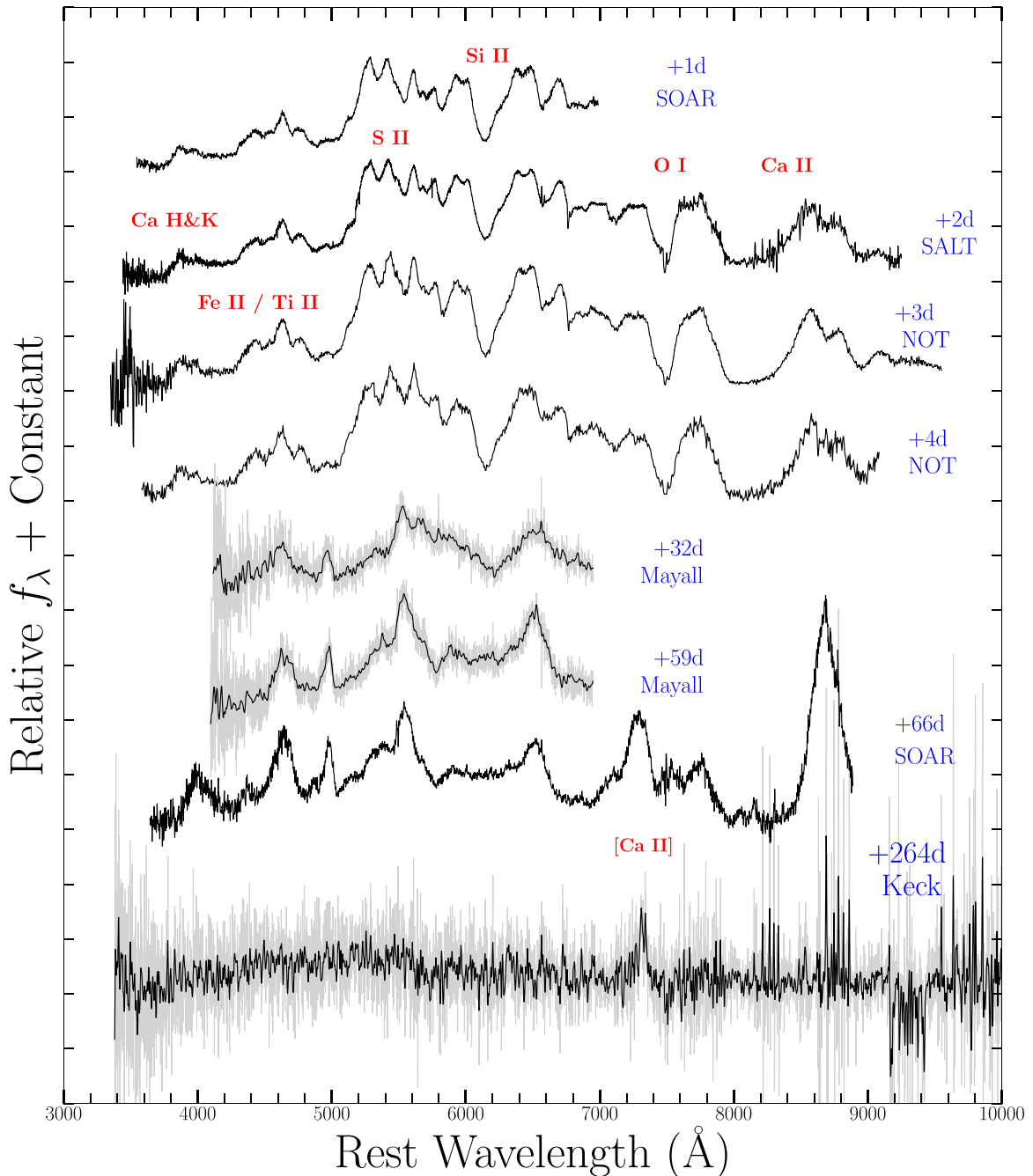
Figure 3. Spectral observations of SN 2016hnk with phases (blue) marked with respect to *B*-band maximum. Raw spectra are shown in gray and spectra smoothed with Gaussian filters in black.

For all spectral observations, standard CCD processing and spectrum extraction were accomplished with IRAF.[14] The data were extracted using the optimal algorithm of Horne (1986). Low-order polynomial fits to calibration-lamp spectra were used to establish the wavelength scale, and small adjustments derived from night-sky lines in the object frames were applied. We employed our own IDL routines to flux calibrate the data and remove telluric lines using the well-exposed continua of

the spectrophotometric standard stars (Wade & Horne 1988; Foley et al. 2003). Details of our spectroscopic reduction techniques are described in Silverman et al. (2012).

SN 2016hnk was last observed by Keck/LRIS on 2017 July 20. At this time the SN had faded significantly and was undetectable in guide camera images, and a blind offset from a nearby star was necessary to acquire the target. In the two-dimensional spectrogram, we did not detect continuum emission from the SN, but did see a broad absorption feature consistent with the wavelength of [Ca II] $\lambda\lambda$7291, 7324. Because of the bright and spatially varying background caused by the SN proximity to the center of its host galaxy, we chose to perform a two-dimensional background subtraction using a

---
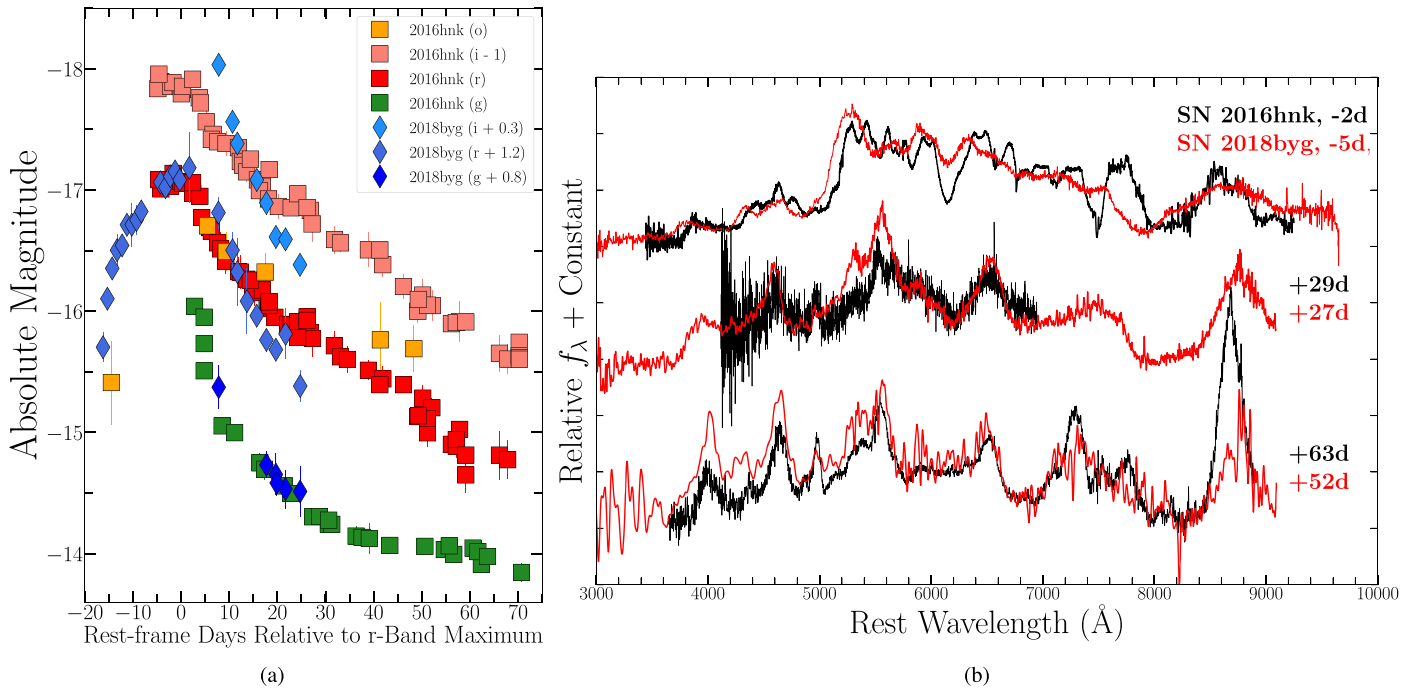
Figure 4. Left: light-curve comparison of *r*- and *g*-band photometry for each object relative to *r*-band maximum. SN 2018byg has been shifted in magnitude to match SN 2016hnk. Right: spectral comparison of SNe 2016hnk and 2018byg at multiple epochs. Phases relative to *r*-band maximum.

third-order Legendre polynomial in the spatial direction. Details of this method can be found in Foley et al. (2009b). While this method produced significantly better results than others attempted, there is still some residual continuum that we believe to be galactic emission.

Additional early-time spectral observations (+2 to 4 days after peak) were retrieved through the WISeREP archive[15] (Yaron & Gal-Yam 2012) and are presented within the complete list of spectral observations in Table A2.

3. Light-curve Analysis

3.1. Photometric Properties

We fit a low-order polynomial to the SN 2016hnk light curve to find best-fit *B*- and *r*-band peak absolute magnitudes of $M_B = -15.40 \pm 0.088$ at MJD 57690.2 ± 0.7 and $M_r = -17.17 \pm 0.04$ at MJD 57693.3 ± 0.6, respectively. We calculate a Phillips (1993) decline parameter value of $\Delta m_{15}(B) = 1.31 \pm 0.085$ mag from our *B*-band light-curve fits. All values are in agreement with those presented in G19.

Based on the ATLAS light curve, the last non-detections in ATLAS cyan and orange filters were at MJD 57667.56 and 57671.55, respectively, with the first detection being in ATLAS-o at MJD 57680.52. We can use these data to constrain the rise time if we match the ATLAS-o observations with all *r*-band data given the similarity in transmission functions of each filter. Consequently, the rise time of SN 2016hnk is in a range of 12.8 days $< t_r <$ 21.8 days. We constrain the rise time further by showing that SN 2016hnk has a faster rise than the 17 days quoted for SN 2018byg (Figure 4(a)) and a similar rise to PTF11kmb (Figure 6(b)), which has $t_r = 15$ days (Lunnan et al. 2017). From this comparison, we estimate a rise time for SN 2016hnk of $t_r = 15 \pm 2$ days.
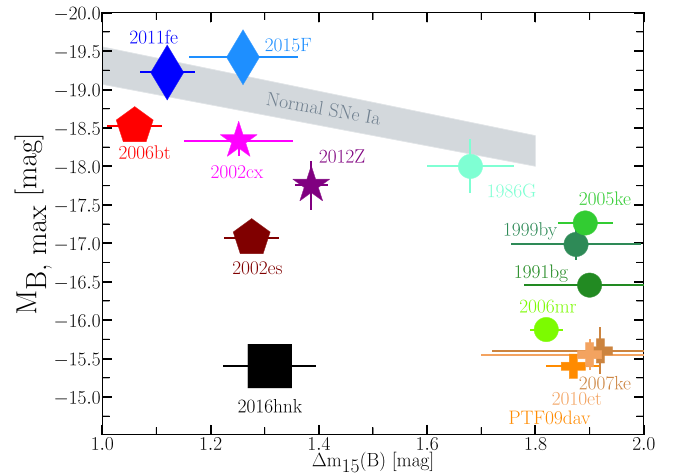

Figure 5. Δm_{15} vs. $M_{B,\mathrm{max}}$ for SN 2016hnk (black square), normal SNe Ia (diamonds + gray region), 91bg-like SNe Ia (circles), SNe Iax (stars), 02es-like SNe Ia (pentagons), and Ca-rich objects (plus signs). Some uncertainties on $M_{B,\mathrm{max}}$ are smaller than plotted marker size.

We present light-curve and spectral comparisons of SNe 2016hnk and 2018byg in Figure 4. In 4(a) we show the parallel between *r*- and *g*-band photometry for these objects. Both SNe exhibit a fast rise time of $\lesssim$17 days, with SN 2016hnk having a slower decline in the *r*-band.

SN 2016hnk has a lower peak M_B than normal SNe Ia as well as sub-luminous SN Ia varieties such as SNe Iax, 91bg-like, and 02es-like objects. SN 2016hnk does have a similar $\Delta m_{15}(B)$ to SNe Iax and SN 2002es, but it is significantly slower fading than other Ca-rich transients and 91bg-like objects. $\Delta m_{15}(B)$ versus M_B comparison of these objects and SN 2016hnk is shown in Figure 5.

We present light-curve comparisons of SN 2016hnk to peculiar thermonuclear SNe in Figure 6. As shown in

---
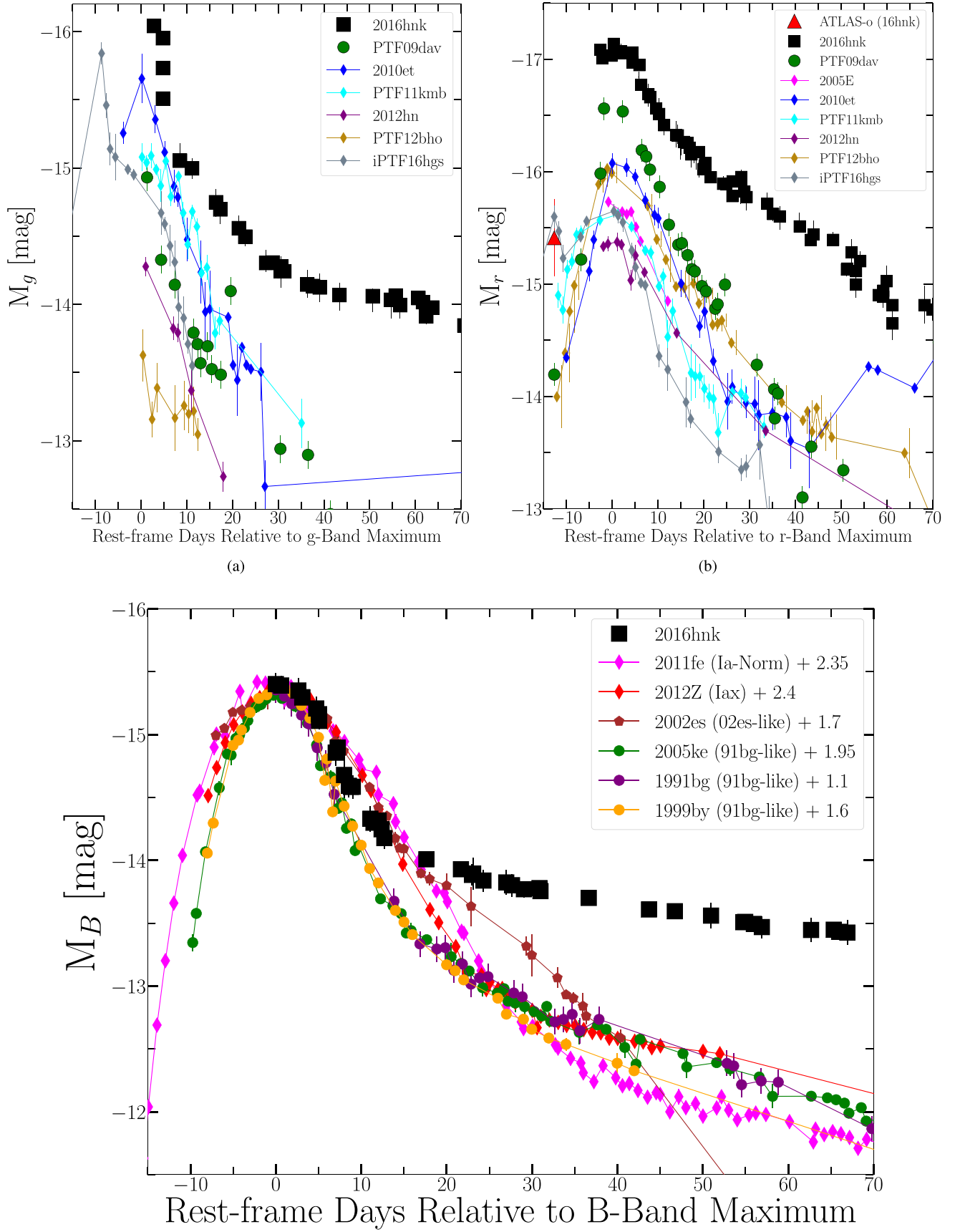
Figure 6. (a) *g*-band comparison of SN 2016hnk and classified Ca-rich transients. (b) *r*-band comparison of SN 2016hnk and known Ca-rich transients. (c) *B*-band comparison of SN 2016hnk and various sub-classes of SNe Ia, all aligned to the $M_{B,\mathrm{max}}$ of SN 2016hnk. The increased flux in SN 2016hnk at $t > 20$ days is unlike anything observed in Ca-rich objects or SNe Ia.

Figures 6(a) and (b), SN 2016hnk is more luminous than Ca-rich transients SN 2005E (Perets et al. 2010), PTF 09dav (Sullivan et al. 2011), SN 2010et (Kasliwal et al. 2012), PTF11kmb (Gal-Yam et al. 2011), SN 2012hn (Valenti et al. 2014), PTF12bho (Kasliwal et al. 2012), and iPTF16hgs (De et al. 2018), in addition to having a slower decline rate. The rise time of these Ca-rich objects is faster than that observed in SN 2016hnk, the most similar objects being SN 2007ke and PTF11kmb, each having a rise time of 15 days (Kasliwal et al. 2012; Lunnan et al. 2017).

Additionally, we present the absolute magnitude B-band light curves of the following SNe Ia with respect to SN 2016hnk: SN 1991bg (Filippenko et al. 1992; Leibundgut et al. 1993), SN 1991by (Garnavich et al. 2004), SN 2002es (Ganeshalingam et al. 2012), SN 2005ke (Gal-Yam 2005), SN 2011fe (Li et al. 2011; Nugent et al. 2011), and SN 2012Z (McCully et al. 2014; Stritzinger et al. 2015). In addition to a difference in peak magnitude, the B-band decline of SN 2016hnk after 20 days is unlike that of normal/sub-luminous SNe Ia or SNe Iax. G19 propose that this late-time light-curve excess could be the result of either a light echo or intervening interstellar material dust at ≈ 1 pc from the explosion site. However, G19 show that there is no evidence of a light echo in SN 2016hnk spectra and the lack of significant changes to the $r - i$ color evolution at these times also disfavors this scenario.

In Figure 7, we present $B - V$, $g - r$, and $r - i$ color comparison plots for SN 2016hnk, Ca-rich transients, and SNe Ia sub-classes. In Figure 7(a), SN 2016hnk's $B - V$ colors are generally redder than all other varieties of normal and sub-luminous SNe Ia as well as SNe Iax. In relation to SNe Ia, SN 2016hnk's $g - r$ and $r - i$ color evolution is also significantly different: SN 2016hnk is ≈ 0.3–0.6 mag redder in $g - r$ and ≈ 0.25–0.5 mag bluer in $r - i$ than even the most similar sub-luminous SNe Ia. Additionally, we present $g - r$ and $r - i$ colors of SN 2018byg as light blue stars in Figures 7(b) and (d). The color evolution of SN 2016hnk is consistent with SN 2018byg to within 0.5 mag in $r - i$ and $g - r$. However, SN 2018byg is slightly redder at most epochs. Comparing to Ca-rich objects, SN 2016hnk is consistent to within 0.2 mag in $g - r$ colors, but is ≈ 0.5 mag bluer than the typical Ca-rich object in $r - i$. As shown by the pink squares in Figure 7, if there were dust reddening from the host galaxy, SN 2016hnk would be even bluer in $r - i$, making it an exceptionally odd object.

3.2. Pseudo-bolometric Light Curve

We construct a pseudo-bolometric light curve for SN 2016hnk using a combination of multi-color optical photometry from Swope, PS1, and LCOGT observations. Luminosities are calculated by trapezoidal integration of SN flux in $BVgriz$ filters (3000–9000 Å). In regions without complete color information, we extrapolate between light-curve data points using a low-order polynomial spline. We present the early-time, pseudo-bolometric light curve in Figure 8(a). For reference, we display models from the Heidelberg Supernova Model Archive[16] that include various binary configurations and explosion mechanisms. We also include an estimated pre-maximum bolometric luminosity at -9.5 days by integrating the pre-maximum brightness spectra

---

[16] https://hesma.h-its.org/doku.php?id=start

of SN 2016hnk and a similar object, SN 2018byg. These spectra are scaled to the first ATLAS-o detection and each phase is relative to r-band peak brightness.

Using the constructed light curve, we find a peak luminosity of $(8.5 \pm 0.5) \times 10^{41}$ erg s^{-1}. This value is smaller than that calculated in G19 who apply a significant host-galaxy reddening correction. We, however, do not apply such a correction because we find no evidence for host extinction (see Section 2.2). We can then use L_{bol} at peak to estimate the total mass of synthesized ^{56}Ni, M_{Ni}, assuming that the radiated luminosity is generated via thermalization of γ-rays from the β-decay of ^{56}Ni $\rightarrow$ ^{56}Co (Arnett 1982). We use the following relation to calculate ^{56}Ni mass:

$$M_{\mathrm{Ni}} = \frac{L_{\mathrm{bol}}}{\gamma \dot{S}(\tau_{\mathrm{r}})} \qquad (1)$$

where τ_{r} is the rise time and γ is the ratio of bolometric to radioactivity luminosities. As in Nugent et al. (1995), we adopt $\gamma = 1.2 \pm 0.2$. $\dot{S}$ is the radioactivity luminosity per solar mass of ^{56}Ni decay:

$$\dot{S} = (6.31 e^{-\tau_{\mathrm{r}}/8.8\,\mathrm{days}} + 1.43 e^{-\tau_{\mathrm{r}}/111\,\mathrm{days}})$$
$$\times 10^{43} \text{ erg s}^{-1} M_{\odot}^{-1}. \qquad (2)$$

Using $\tau_{\mathrm{r}} = 15 \pm 2$ days (Section 3.1), we calculate $M_{\mathrm{Ni}} = 0.03 \pm 0.01\,M_{\odot}$. This value is consistent to 1σ with that reported for PTF09dav ($0.019 \pm 0.003\,M_{\odot}$; Sullivan et al. 2011) and consistent to $\sim 2\sigma$ with the lowest-luminosity 91bg-like object, SN 2007ax ($0.038 \pm 0.008\,M_{\odot}$). The total ^{56}Ni mass mass in SN 2016hnk is also lower than that found for SN 2018byg ($\approx 0.11\,M_{\odot}$; De et al. 2019), which is consistent with the observed difference in luminosity between the two objects at peak. The total ^{56}Ni mass in SN 2016hnk is still significantly less than the majority of sub-luminous SNe Ia.

We then use the relation from Foley et al. (2009a) to estimate the ejecta mass of SN 2016hnk:

$$M_{\mathrm{ej}} = 0.16 \left(\frac{\tau_{\mathrm{r}}}{10\,\mathrm{days}} \right)^2 \left(\frac{0.1\,\mathrm{cm}^2\,\mathrm{g}^{-1}}{\kappa} \right) \left(\frac{v}{2 \times 10^8\,\mathrm{cm\,s}^{-1}} \right) \quad (3)$$

where κ is the opacity and v is the ejecta velocity. Using a standard SN Ia opacity of 0.2 cm^{2}g^{-1} and a calculated ejecta velocity of $-10{,}300$ km s^{-1} from Si II absorption, we find $M_{\mathrm{ej}} = 0.9 \pm 0.3\,M_{\odot}$. Given the strength of Ca II in the SN 2016hnk spectra, the true opacity could be larger than a normal SN Ia, which in turn would yield a smaller ejecta mass than our current estimate.

We also examine the decline of the pseudo-bolometric light curve at late times to check the consistency with standard ^{56}Co decay. As shown in Figure 8(b), the lack of multi-filter photometric data after ~ 100 days makes it difficult to calculate precise late-time bolometric luminosities for SN 2016hnk. However, we can place an estimate on the bolometric luminosity by scaling nebular spectra of SN 2016hnk and similar objects to the Keck I-band flux at $+291$ days. If we first assume that all the flux at late times is derived from [Ca II] emission, we can scale the Keck LRIS spectrum at $+264$ days to the I-band flux and integrate over the wavelength range of the Keck I-band transmission function. With this method, we calculate a luminosity of $2.2 \pm 0.90 \times 10^{39}$ erg s^{-1} (red star in Figure 8(b)). The phase of the Keck spectrum and the I-band

(a)

(b)

(c)

(d)

(e)
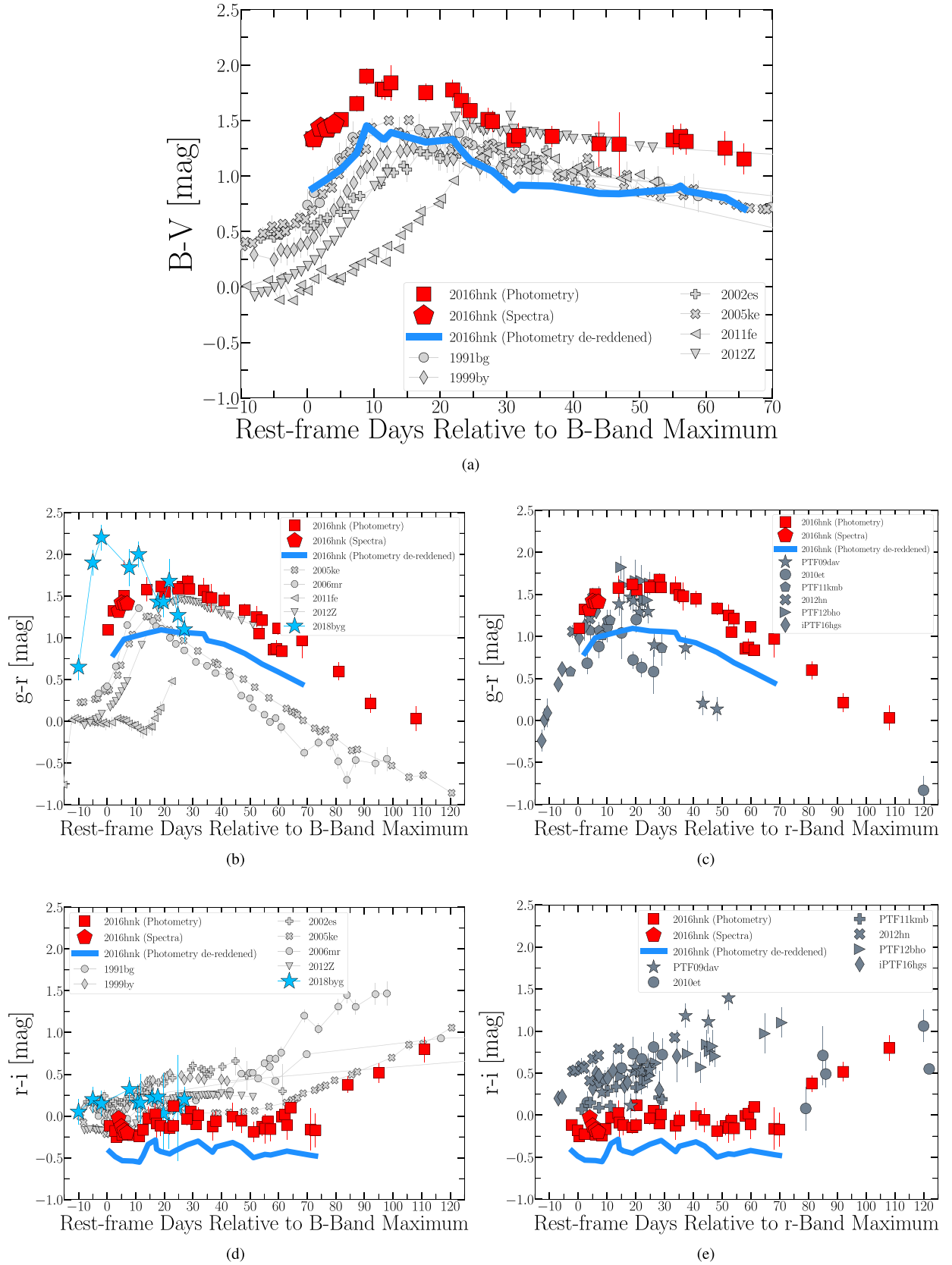
Figure 7. (a) $B - V$ color comparison of SN 2016hnk and various types of SNe Ia. SN 2016hnk colors from photometry are presented as red squares and colors from spectra as red polygons. The blue line represents the photometric colors that have been de-reddened to match SNe Ia color curves. With this artificial de-reddening, SN 2016hnk does not match any SNe Ia in $r - i$. (b) $g - r$ color comparison of SN 2016hnk and assorted SNe Ia. SN 2018byg is shown as light blue stars. (c) $g - r$ color comparison of SN 2016hnk and Ca-rich transients. (d) $r - i$ color comparison of SN 2016hnk and different SNe Ia. (e) $r - i$ color comparison of SN 2016hnk and Ca-rich transients.
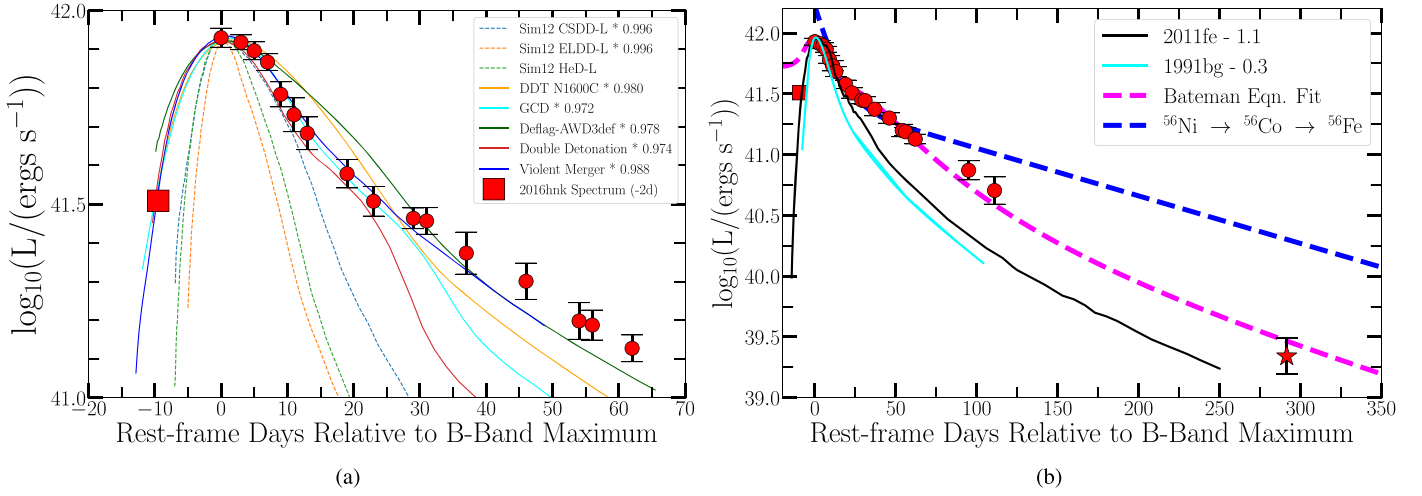
Figure 8. (a) Early-time pseudo-bolometric light curve of SN 2016hnk. The detection luminosity has been estimated using the ATLAS o-band observation and pre-maximum spectra of SNe 2016hnk and 2018byg. Spectral phases are relative to r-band maximum and plotted with respect to the B-band. We also show explosion models from the Heidelberg group for reference. (b) Full pseudo-bolometric light curve of SN 2016hnk with the ∼300 day luminosity estimate calculated using the Keck I-band detection and nebular spectra from a similar phase. Pseudo-bolometric light curves of SN 1991bg and 2011fe are shown in cyan and black, respectively (Stritzinger et al. 2006; Zhang et al. 2016). The Bateman equation fit is shown in magenta, while the standard ^{56}Co decay with complete γ-ray trapping shown in blue.

detection are not identical, but this does not add extra uncertainty on the luminosity if we assume that the spectral evolution between epochs is small. Additional uncertainties on this measurement originate from the lack of photometric detections in other Keck filters; this may indicate additional flux outside of the I-band transmission curve. However, we consider this unlikely given that the only detectable feature in the Keck spectrum is [Ca II]. We place additional constraints on SN 2016hnk's bolometric decline by estimating its luminosity using SNe Iax 2002cx and 2008A, which have a similar Ca-dominated spectral composition at nebular times. Scaling the spectra of these objects at a similar phase to the Keck I-band flux, we calculate additional bolometric luminosities for SN 2016hnk. Luminosities from 2002cx and 2008A SEDs are within the errorbars present in 8(b).

We then use our estimates for the late-time bolometric luminosity of SN 2016hnk to explore the standard ^{56}Ni-powered decline that is typically observed in SNe Ia. As shown in Figure 8(b), the bolometric decline of SN 2016hnk is slower than that of SN 2011fe (black; Zhang et al. 2016) and SN 1991bg (cyan; Stritzinger et al. 2006). The SN 2016hnk decline rate is also inconsistent with a simple ^{56}Co → ^{56}Fe decay (i.e., complete γ-ray trapping) as presented by the dashed blue line in 8(b).

We model the radioactive decay-powered light curve using a similar method to late-time studies of SNe Ia (Seitenzahl et al. 2013; Graur et al. 2016; Dimitriadis et al. 2017; Shappee et al. 2017; Jacobson-Galán et al. 2018). We employ the Bateman equation to fit the bolometric decline produced by radioactive isotopes:

$$L_A(t) = 2.221 \frac{\lambda_A}{A} \frac{M(A)}{M_\odot} \frac{q_A^x + q_A^l f_A^l(t) + q_A^\gamma f_A^\gamma(t)}{keV}$$
$$\times \exp(-\lambda_A t) \times 10^{43} \text{ erg s}^{-1} \qquad (4)$$

where t is time since explosion, λ_A is the decay constant, A is the atomic number, and q^l, q^γ, and q^x are the average energies of charged leptons, γ-rays, and X-rays, respectively, per decay. All decay energies and constants are as presented in Table 2 of

Seitenzahl et al. (2014). We assume complete trapping of energy deposited by charged leptons (i.e., $f_A^l = 0$) and do not include X-ray energies in our fits. We use the following expression for γ-ray trapping:

$$f_A^\gamma = 1 - \exp\left[-\left(\frac{t_A^\gamma}{t}\right)^2\right] \qquad (5)$$

where t_A^γ is the γ-ray trapping timescale for a given radioactive isotope produced in the explosion (Woosley et al. 1989; Seitenzahl et al. 2014).

In our model, we fit for the mass and γ-ray trapping timescale of ^{56}Co as well as the mass of ^{57}Co. However, the luminosity contribution is dominated by synthesized ^{56}Co until ≈300 days after explosion, thus making the ^{57}Co contribution negligible on this timescale. Modeling the data with Equation (4), we find ^{56}Co and ^{57}Co masses of 0.029 ± 0.001 and ≈0 $M_\odot$, respectively. This result is consistent with our total ^{56}Ni mass estimate of $M_{Ni} = 0.03 \pm 0.006 M_\odot$. We also calculate a trapping timescale of $t_{56}^\gamma = 60.06^{+4.12}_{-3.71}$ days. We display our model fit as the dashed magenta line in Figure 8(b).

4. Spectral Analysis

4.1. Line Identification

We model the early-time spectra of SN 2016hnk with the spectral synthesis code SYNAPPS (Thomas et al. 2011) in order to understand the elements produced in the explosion. SYNAPPS is utilized primarily for line identification and relies on generalized assumptions about the SN such as spherical symmetry, local thermal equilibrium (LTE), and homologous expansion of ejecta. As shown in Figure 9(a), we identify the following species most commonly found in thermonuclear SNe: O I, Si II, S II, Ca II, Ti II, Fe II/III, and Co I/II. We do not detect C I nor Mg I in our fits and the detection of Na I is probable but not definite. We also find no detectable He I in any SYNAPPS modeled spectra. This finding is unlike other Ca-rich objects, which typically show clear signatures of photospheric helium near peak.

(a)

(b)
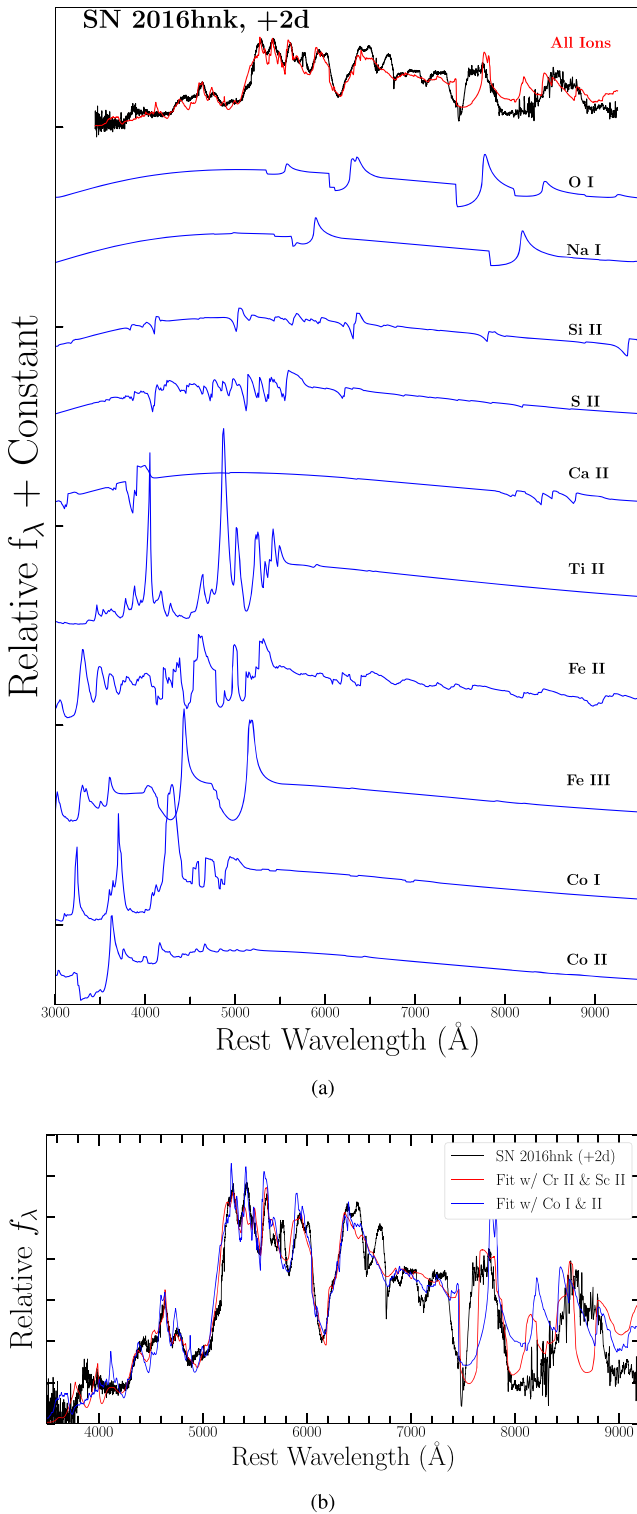
Figure 9. (a) Decomposition of active ions in the SYNAPPS fit; phase relative to *B*-band maximum. The total fit is shown in red, while blue lines mark each individual ion's contribution. (b) Similar SYNAPPS fits to SN 2016hnk. In red, the fit includes all active ions shown in (a) except with Sc II and Cr II instead Co I and Co II.

We ran various SYNAPPS fits in an attempt to identify more exotic elements such as Cr II, Sc II, and Sr II, all of which are claimed to be robustly detected in SYNAPPS models of PTF09dav by Sullivan et al. (2011). We present a model comparison in Figure 9(b) of a fit including typical
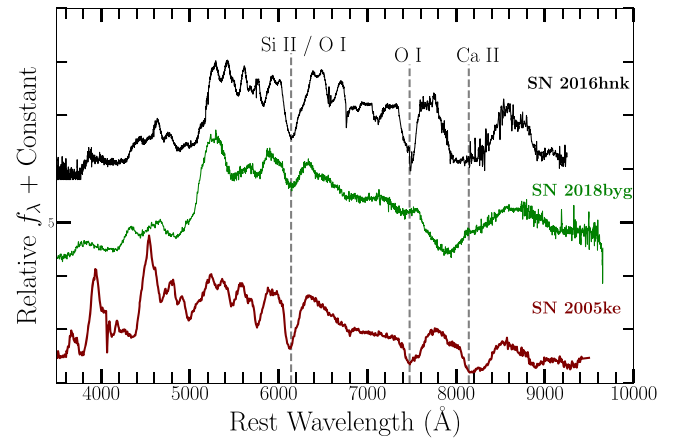
Figure 10. Spectral comparison of SNe 2016hnk (black), 2018byg (green), and 2005ke (maroon) at similar phases near peak magnitude. SNe 2016hnk and 2018byg have significant blueward line blanketing among Fe-group elements and higher-velocity Ca II absorption than 91bg-like SN 2005ke.

thermonuclear species (e.g., Fe II/III, Ti II, Co I/II; (blue line)) and a fit with both typical species (e.g., Fe II/III and Ti II; (red line)) in additional to exotic species (e.g., Cr II and Sc II). The two line profiles at $\lambda\lambda5400, 5550$ are more accurately fit with blends of S II and Fe-group elements than Sc II. We also find that adding Cr II does not improve our SYNAPPS fits. Despite the visual similarities between near-peak spectra of SN 2016hnk and PTF09dav, we cannot place the same level of confidence on the detection of Sc II, Cr II, and Sr II in SN 2016hnk as Sullivan et al. (2011) did for PTF09dav.

4.2. Spectral Comparisons

SN 2016hnk is extremely similar to SN 2018byg at each phase of spectroscopic observations presented in 4(b). At similar phases near maximum light, both objects contain broad, high-velocity Ca II absorption features with velocities of $-17151.41 \pm 540.10\,\mathrm{km\,s^{-1}}$ in SN 2016hnk and $-22221.70 \pm 706.0\,\mathrm{km\,s^{-1}}$ in SN 2018byg. Ca II and Si II velocities were calculated by fitting the minimum of each absorption feature using a low-order polynomial. A more complete velocity evolution for both objects is presented in Figure 18. Furthermore, the spectra of SNe 2016hnk and 2018byg both show suppressed emission from line blanketing of Fe-group elements. As indicated by the colors shown in Figure 7, SN 2016hnk's "redder" $B - V$ colors with respect to its "bluer" $r - i$ colors are the result of this blueward line blanketing. This characteristic is unique to these two SNe and sets them apart from other sub-luminous thermonuclear objects such as 91bg-like objects (Figure 10).

Spectroscopic differences between the two objects include higher overall elemental velocities in SN 2018byg and deeper Si II/O I absorption in SN 2016hnk. There are no published nebular spectra of SN 2018byg to compare with our late-time SN 2016hnk spectral observations.

Initial spectral classifications of SN 2016hnk noted similarities between both sub-luminous, 91bg-like objects as well as the Ca-rich transient PTF09dav. We show a time-series spectral comparison in Figure 11. As shown in Figure 11(a), SN 2016hnk has matching Si II, O I, and Ca II absorption to 91bg- and 02es-like objects. Similar features are also observed in PTF09dav, but with slower expansion velocities than those in the SN 2016hnk spectra. Fe II/III emission and Ti II
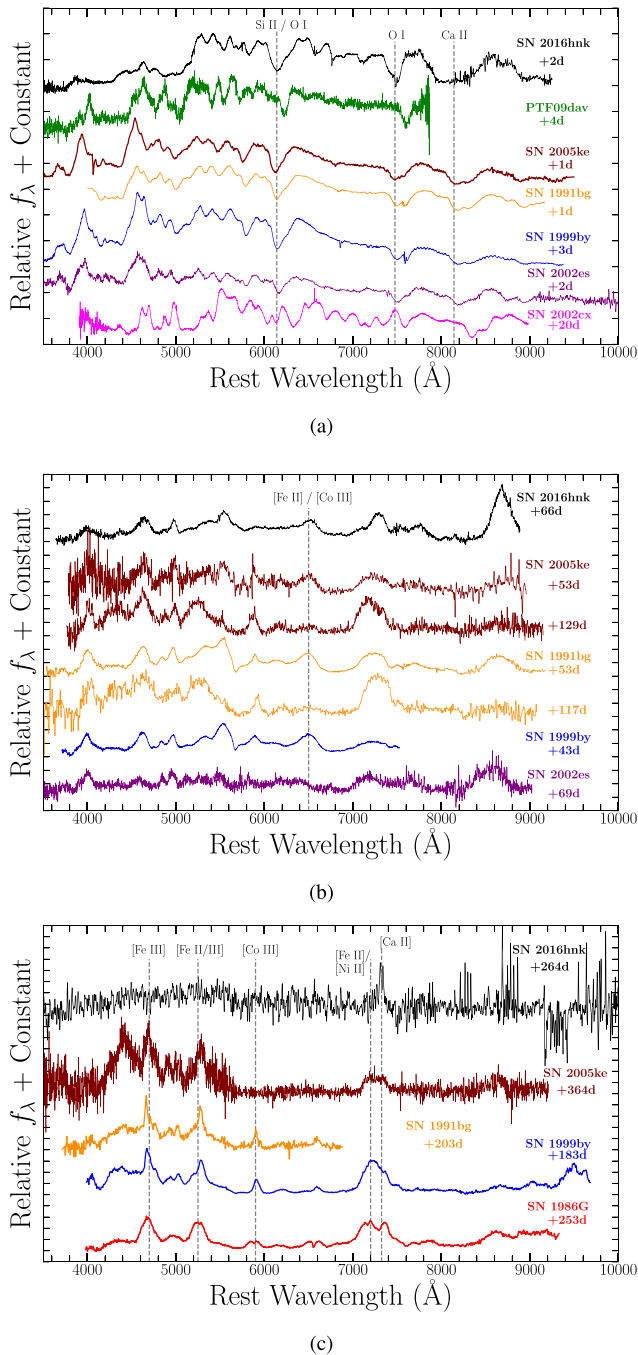
Figure 11. (a) Early-time spectral comparison of SN 2016hnk, PTF09dav, and assorted sub-luminous SNe Ia. All phases are with respect to B-band maximum. (b) Pre-nebular spectral comparison of SN 2016hnk and sub-luminous SNe Ia. (c) Comparison of nebular spectra of SN 2016hnk and 91bg-like objects at approximately the same phase. The SN 2016hnk spectrum (black) has been smoothed.

absorption profiles are shared between both objects. SN 2016hnk, however, has significantly suppressed emission in blue wavelengths compared to PTF09dav.

The primary differences between SN 2016hnk and other sub-luminous SNe Ia are the relative velocities and the prominence of Fe-group elements. While the Si II velocity of SN 2016hnk does match 91bg-like objects, the Ca II in SN 2016hnk is moving $\sim 7000\,\mathrm{km\,s^{-1}}$ faster than the velocities observed in "91bg-like" SNe 1991bg ($10350 \pm 380\,\mathrm{km\,s^{-1}}$), 1999 by ($9290 \pm 450\,\mathrm{km\,s^{-1}}$), and 2005ke

($11100 \pm 680\,\mathrm{km\,s^{-1}}$) near peak. This variation in Ca II velocity suggests a different explosion mechanism for SN 2016hnk than that of 91bg-like objects. Furthermore, at early times, the observed line blanketing of Fe-group elements in the SN 2016hnk spectra is not observed in other comparison objects presented in Figure 11(a).

Despite the similar prevalence of [Ca II] lines in the nebular phase, the dominance of Fe-group elements in 91bg-like objects is not observed in the Keck spectrum of SN 2016hnk at +264 days. As shown in Figure 11(c), the nebular spectra of all 91bg-like objects have prominent [Fe II], [Fe III], and [Co II] emission features in blue wavelengths. These features are not present in the SN 2016hnk spectrum at a similar phase, which suggests that significantly less ^{56}Ni was synthesized during explosion. This observed contrast is supported by SN 2016hnk's low peak luminosity as compared to other sub-luminous SN Ia varieties. Furthermore, the [Ca II] profile in SN 2016hnk is much narrower than that shown in the 91bg-like objects, all of which possess a blend of [Ca II] and [Ni II] emission at $\sim 7300\,\text{Å}$.

Nebular spectra of SN 2016hnk does show some similarities to observations of other Ca-rich objects at late times. In Figure 12, we present SN 2016hnk spectra at +66 days and +264 days in relation to most nebular spectra of Ca-rich transients. There is a noticeable parallel between the [Ca II] emission features in all presented objects, in addition to the minor or non-existent presence of Fe-group elements. [Ca II] line profiles are similar in all objects and do not show significant [Ni II] line blending. Like PTF09dav, SN 2016hnk does not have detectable [O I] and is thus significantly more O-poor than other objects such as 2003dr, 2005E, PTF11kmb, and 2012hn. We present direct comparison of [O I] and [Ca II] line profiles in Figure 13(a). Furthermore, SN 2016hnk does not show narrow Hα emission at late times as is detected in PTF09dav.

We compare the [Ca II]/[O I] ratio of SN 2016hnk to all Ca-rich objects and Type Ibc/IIP/IIb SNe in 13(b). Given the lack of observed [O I] in both objects, PTF09dav and SN 2016hnk have the highest [Ca II]/[O I] ratio with respect to other SNe. This indicates a relatively O-poor explosion for both PTF09dav and SN 2016hnk as compared to most other Ca-rich objects.

These spectroscopic comparisons have demonstrated that SN 2016hnk is most similar to SN 2018byg given its observed blueward line blanketing and its strong, high-velocity Ca II features. SN 2016hnk has some similar line profiles to 91bg-like SNe (e.g., Si II and S II), but has significantly faster Ca II velocities and substantial line blanketing than this sub-class of SNe Ia. SN 2016hnk also has weaker Fe-line transitions than these objects at nebular times. Like other Ca-rich transients, the nebular spectra of SN 2016hnk is dominated by [Ca II] emission. While the ratio of [Ca II]/[O I] line fluxes for Ca-rich transients is typically greater than 2, this ratio for SN 2016hnk and PTF09dav is almost twice that of typical Ca-rich objects. This suggests either stronger calcium emission in SN 2016hnk or a limited oxygen presence in this SN than Ca-rich SNe.

4.3. Comparison to SNe Iax Nebular Spectra

As shown in Figure 14, SN 2016hnk's [Ca II] emission profile is quite similar to that found in nebular phase spectra of SNe Iax. Also "Ca-rich" at late times, SNe Iax exhibit strong [Ca II] and variable [Fe II]/[Ni II] emission features, both of which are tracers of initial WD mass and the possible wind from a bound SN remnant (Foley et al. 2016). Unlike most
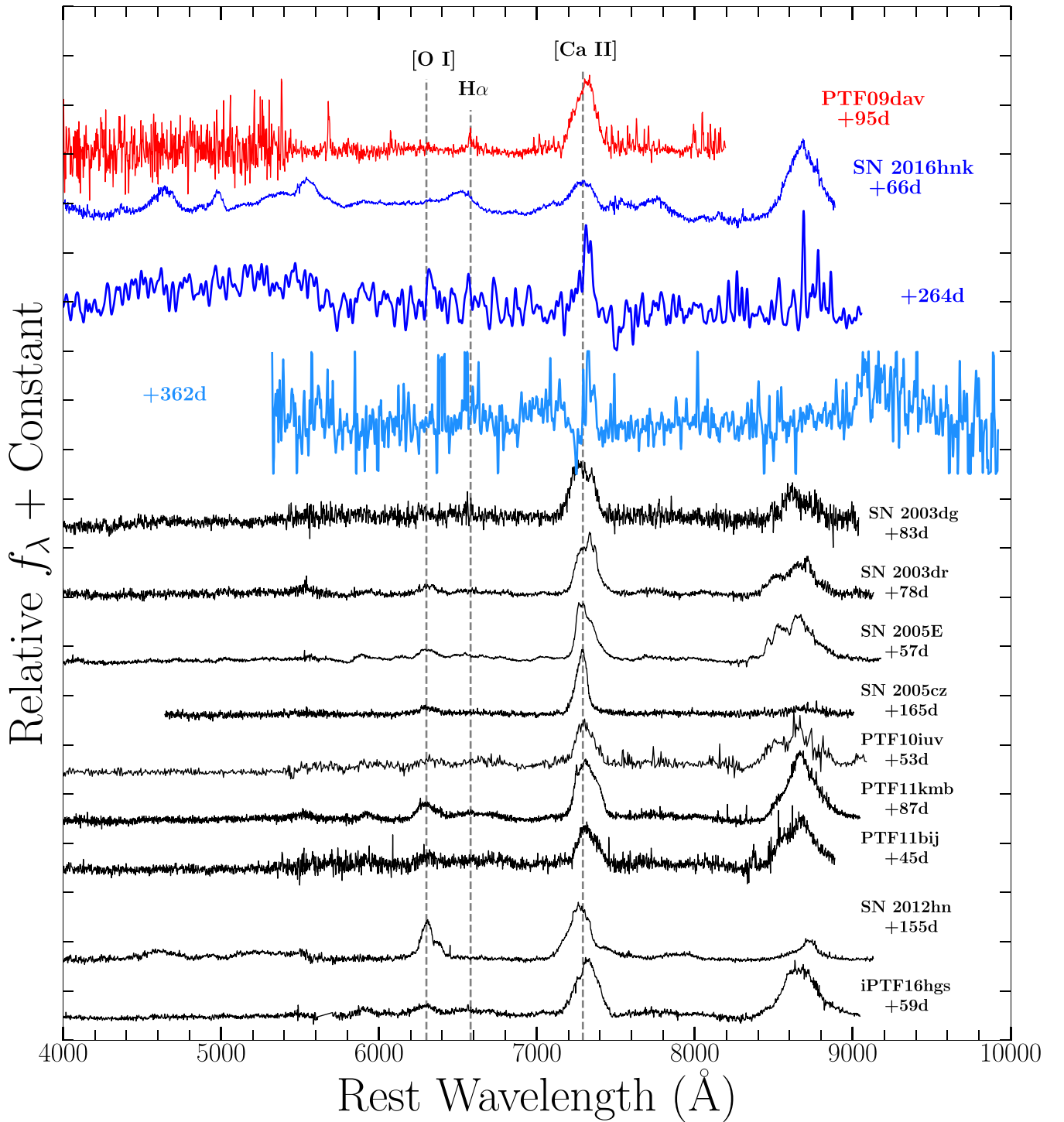
Figure 12. Nebular spectra of all classified "Ca-rich" transients. The nebular spectra of PTF09dav and SN 2019hnk are shown in red and blue, respectively. Note that the +66 day spectrum of SN 2016hnk is still photospheric and thus cannot be directly compared with Ca-rich objects at a similar phase. The +264 day spectrum of SN 2016hnk has been smoothed with a Gaussian filter. The light blue +362 day spectrum has also been smoothed and was presented originally in G19. Prominent [O I] and [Ca II] lines are marked by vertical dashed gray lines.

SNe Iax, SN 2016hnk does not have visible [Ni II] emission, which suggests that there are very few stable nickel isotopes, such as ^{58}Ni, present in the ejecta. This is indicative of a sub-Chandrasekhar explosion in which the WD density is too low for sufficient electron capture. This conclusion is supported by our ejecta mass estimate of $\sim 0.9\,M_\odot$ (Section 3.2). Further-more, as shown in Foley et al. (2016), narrow forbidden lines in nebular spectra may result from wind from a bound remnant.

Such a model could be a viable explanation for SN 2016hnk at late times given its [Ca II] profile shape is consistent with SNe Iax such as 2008A and 2010ae.

4.4. Stripped Mass Calculation

The single-degenerate (SD) progenitor channel involves a WD in a binary system with a non-degenerate companion star.

(a)

(b)

(c)
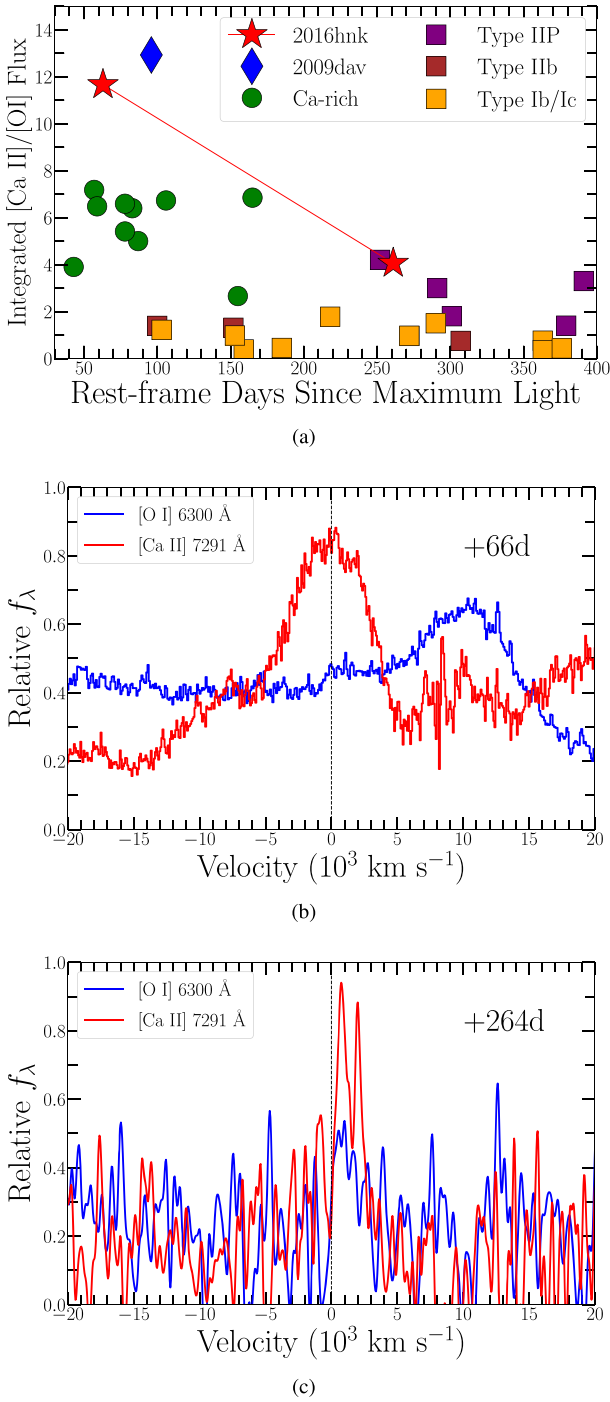
Figure 13. (a) Ratio of integrated [Ca II] and [O I] flux with respect to phase for SN 2016hnk, PTF09dav, Ca-rich transients, and assorted types of core-collapse SNe; [Ca II]/[O I] values for all Type II/Ibc objects from Milisavljevic et al. (2017). (b)/(c) Velocity profiles of [O I] $\lambda\lambda6300$, 6364 (blue) and [Ca II] $\lambda\lambda7291$, 7324 (red) in SN 2016hnk at +66 days and +264 days, respectively.

In this scenario, it is predicted that ablated H- or He-rich material from the non-degenerate companion will be swept up by the SN ejecta and should be detectable in late-time spectra as narrow emission lines with velocities of $\approx1000\,\mathrm{km\,s^{-1}}$ (Marietta et al. 2000; Mattila et al. 2005; Liu et al. 2012, 2013a; Pan et al. 2012; Lundqvist et al. 2013). We test this scenario by calculating upper limits on the mass of stripped hydrogen and helium potentially present in the nebular spectrum of SN 2016hnk.
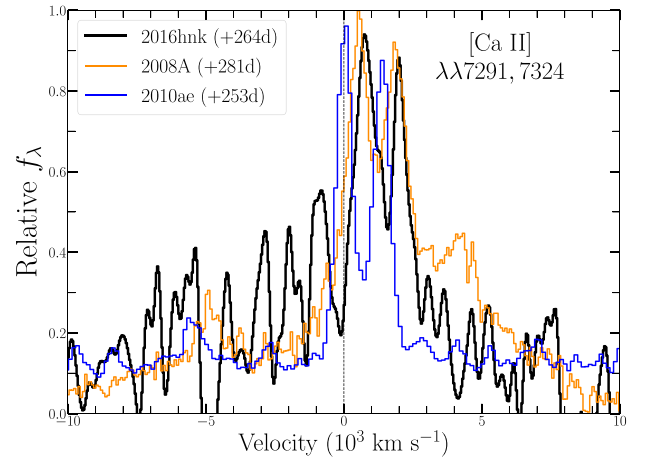
Figure 14. [Ca II] $\lambda\lambda7291$, 7324 velocity profiles of SN 2016hnk (black) and SNe Iax, 2008A (orange) and 2010ae (blue) at similar phases. Like SN 2016hnk, SNe Iax are also Ca-rich in nebular phases and their [Ca II] emission may be a signature of wind from a bound remnant (Foley et al. 2016).

We preface this analysis by stating that all stripped mass models used have been designed specifically for SNe Ia and not Ca-rich or low-luminosity thermonuclear objects. Thus these models are most notably different from SN 2016hnk in their energetics and total Ni mass produced, in addition to possible asymmetries. Consequently, the lower overall energies and SN densities in Ca-rich objects may affect the mixing of H/He circumstellar material, but the differences in Ni mass between each SN type will scale with the luminosity. Nonetheless, these models and radiative transfer simulations are applicable to this analysis as a means of testing an SD companion interaction scenario for SN 2016hnk.

We visually examine the +264 day nebular spectrum of SN 2016hnk and find no obvious detections of narrow Hα or He I emission. We do, however, observe a narrow feature near $\lambda6563$ in the nebular spectrum, which has a FWHM velocity of $203.65 \pm 55.8\,\mathrm{km\,s^{-1}}$. This velocity is low for SN-related material, e.g., the Hα emission in PTF09dav has a velocity of $1315.17 \pm 241.05\,\mathrm{km\,s^{-1}}$. Furthermore, this feature does not have significant signal-to-noise ratio compared to the overall spectral noise. Therefore we perform the analysis of potential ablated material by assuming a non-detection of nebular Hα emission.

To calculate the stripped hydrogen luminosity limit, we simulate a marginal detection by modeling the Hα emission as a Gaussian profile (FWHM = $1000\,\mathrm{km\,s^{-1}}$) with a peak flux of three times the spectrum's root mean square (rms) flux (Sand et al. 2018; Dimitriadis et al. 2019). We present the simulated limit for marginal detection of Hα emission in Figure 15(a).

We use the 3σ flux limit for marginal detection to calculate the luminosity limit of stripped hydrogen in the nebular spectrum. We then convert the Hα luminosity to stripped mass using the following relation from Botyánszki et al. (2018):

$$\log_{10}(L_{\mathrm{H}\alpha}) = -0.2M_1^2 + 0.17M_1 + 40, \qquad (6)$$

where $L_{\mathrm{H}\alpha}$ is the Hα luminosity in cgs units at 200 days after peak, $M_1 = \log_{10}(M_{\mathrm{H}}/M_\odot)$, and M_{H} is the stripped hydrogen mass. We re-scale our estimated Hα luminosity limit because this relation is derived at exactly 200 days after peak. We calculate the decline in luminosity of SN 2016hnk to be a factor of 4 between 200 and 300 days. We find a Hα luminosity
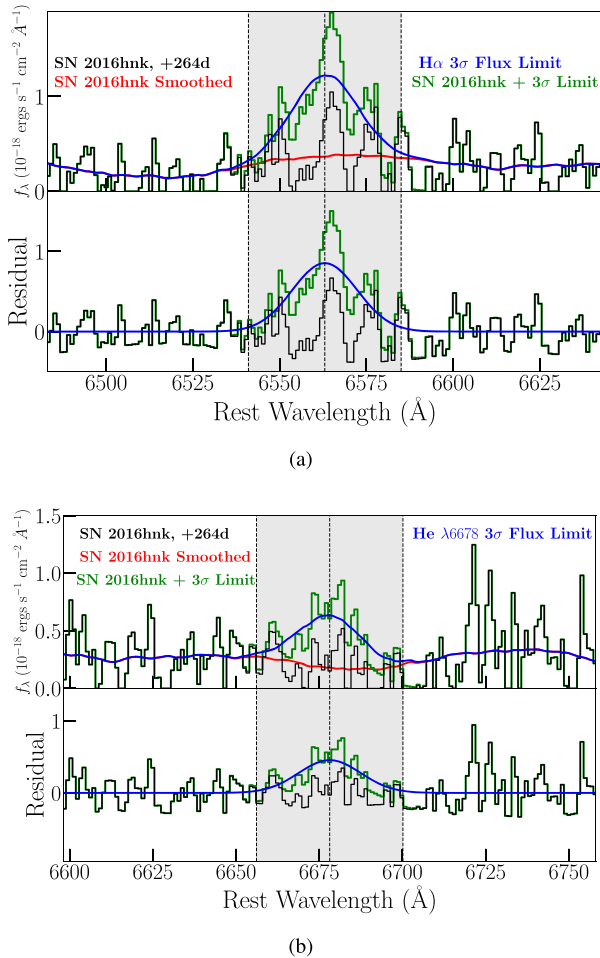
Figure 15. (a) Upper panel: in black, flux-calibrated late-time data of SN 2016hnk at +264 days with no apparent Hα emission. Shown in red is the continuum that has been smoothed with a Savitzky–Golay filter. The 3σ rms flux limit for marginal detection of Hα is shown in blue. The data plus 3σ flux limit is shown in green. The gray shaded region represents a wavelength range of 22 Å ($\sim$1000 km s^{-1}). Lower panel: in green, residuals of data plus the 3σ limit, minus smoothed data. In black, residuals of data minus smoothed continuum; Hα 3σ flux limit shown in blue. (b) Same method as for Hα, but with marginal detection of the 6678 Å He I emission line.

limit luminosity limit of $L_{\mathrm{H}\alpha} < 1.3 \times 10^{38}$ erg s^{-1}, which corresponds to $4.6 \times 10^{-3}\,M_\odot$ of undetected, stripped H-rich material in SN 2016hnk. This mass is an order of magnitude lower than model predictions for stripped H-rich material that is swept-up by an SN Ia in a Roche-lobe-filling progenitor system (1.4×10^{-2} to $0.25\,M_\odot$; Liu et al. 2012; Pan et al. 2012; Boehner et al. 2017).

To calculate the limit of stripped helium in SN 2016hnk, we mimic the procedure outlined in Jacobson-Galán et al. (2019) for He I $\lambda6678$. Our marginal detection calculation follows the same procedure as Hα and we display the 3σ limit for He I emission in Figure 15(b). As shown in Figure 4 of Botyánszki et al. (2018), the MS38 model produces an Hα emission line that is $\sim$5 times more luminous than He I $\lambda6678$. Because of this, we modify Equation (6) to have the following form:

$$\log_{10}(L_{\mathrm{He}}) = -0.2M_1^2 + 0.17M_1 + 39.3, \qquad (7)$$

where $M_1 = \log_{10}(M_{\mathrm{He}}/M_\odot)$ and M_{He} is the stripped helium mass. We calculate a stripped helium luminosity limit of

$L_{\mathrm{He}} < 6.8 \times 10^{37}$ erg s^{-1} and a corresponding maximum stripped mass of $1.2 \times 10^{-2}\,M_\odot$ found using Equation (7). In SD He-star companion interaction models, the predicted ranges of stripped He-rich masses are 2.5×10^{-3}–$1.3 \times 10^{-2}\,M_\odot$ (Pan et al. 2012) and 9.5×10^{-3}–$2.8 \times 10^{-2}\,M_\odot$ (Liu et al. 2013b), both of which are consistent with the helium mass limit of SN 2016hnk.

5. Explosion Models

The observed spectroscopic and photometric properties of SN 2016hnk suggest a different explosion scenario than typical sub-luminous SNe Ia. The prominence of high-velocity ($v \sim 18{,}000$ km s^{-1}), intermediate-mass elements such as Ca II in SN 2016hnk indicates a potential helium detonation (Fink et al. 2010; Kromer et al. 2010). Such a scenario can produce a large amount of Fe-group elements in the outer regions of the SN ejecta that causes significant line blanketing near maximum light, in addition to a fast-rising light curve (Shen et al. 2018; Polin et al. 2019a). These expected signatures of helium shell detonation on a C/O WD are consistent with the observed spectral features and light-curve evolution of SN 2016hnk.

We model the light curve and spectra of SN 2016hnk with a grid of different helium shell detonation scenarios derived from Polin et al. (2019a). Our simulations track the double detonation of a 50% carbon + 50% oxygen, $\sim$0.8 $M_\odot$ WD with $\sim$0.03 $M_\odot$ of helium on the surface. Each progenitor profile is constructed using a semi-analytic method which ensures the WD and helium shell of our chosen masses begin in hydrostatic equilibrium (Zingale et al. 2013). We then use the Eulerian hydrodynamics code `Castro` (Almgren et al. 2010) to follow each simulation's hydrodynamical evolution and nucleosynthetic reactions from initial helium ignition through homologous expansion. Once the ejecta have reached homology we generate synthetic light curves and spectra from each model using the radiative transfer code `Sedona` (Kasen et al. 2006).

In Figures 16(a)/(b), we compare the helium shell model light curves to our V-, g-, r-, i-band photometry. We find that helium shell detonation with a total mass of 0.87 $M_\odot$ (WD + helium shell) can reproduce the peak absolute magnitudes in all bands as well as the early-time light-curve decline. The first, ^{48}Cr-powered, light-curve peak is eliminated when the mixing of outer ejecta is included in our models. Such a model (N100) is presented as a dotted line in Figure 16(a) and includes mixing of 0.1 $M_\odot$ of outer ejecta. The mixing of outer ejecta produces a slightly better fit to some photometric observations, but additional constraints cannot be placed on the very early-time light-curve evolution due to the limited pre-maximum data for SN 2016hnk. However, we do include ATLAS-o- and -c-band data for comparison with r/i- and V-bands, respectively. The pre-maximum o-band data point in Figure 16 appears to be most consistent with the best-fitting, non-mixed 0.85 + 0.02 shell model (green line), but it is also within the phase uncertainties of the 0.85 + 0.02 mixed N100 model (dotted violet–red line).

The divergence between the models and SN 2016hnk at $\sim$25 days post-explosion may be attributed a variety of factors within the explosion. First, for a similar model, the LTE assumptions within the `Sedona` code may be less representative of the conditions within the ejecta of SN 2016hnk than in SN 2018byg, which is modeled to have a higher total mass
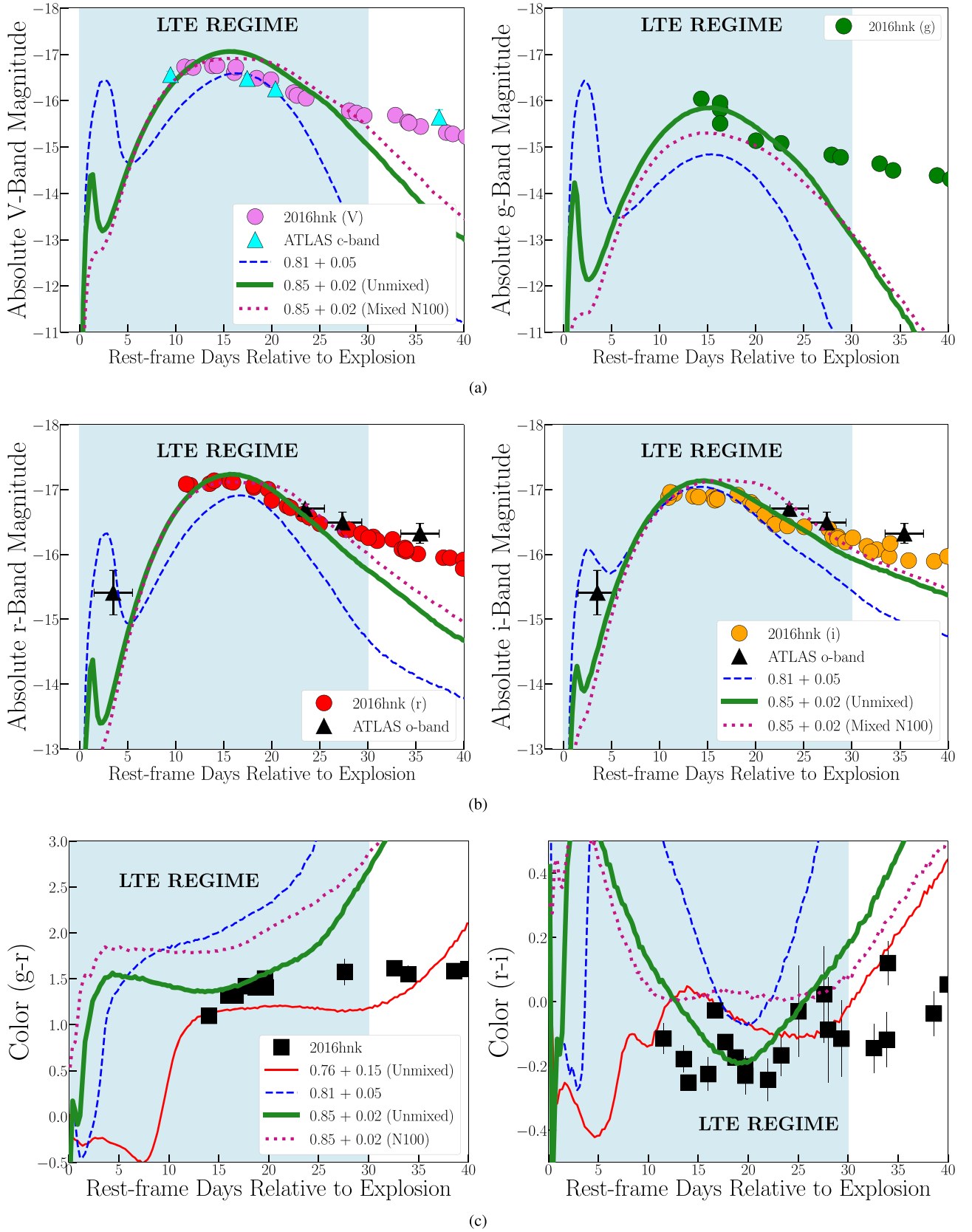
Figure 16. (a)/(b) Light-curve comparison to double-detonation helium shell models presented in Polin et al. (2019a). The local thermal equilibrium regime (i.e., where the models are most reliable) is shown by the shaded light blue region. The best-fitting 0.85 + 0.02 model has no mixing of ejecta and is shown in forest green. The same model but with mixing (N100) is shown in violet–red. Left to right: V-, g-, r-, i-band photometry. ATLAS photometry is included for early-time light-curve information. We put errorbars on the phases of the ATLAS data to illustrate that the date of explosion is uncertain to within ∼2 days for all photometry. (c) g − r and r − i color comparison to helium shell models.
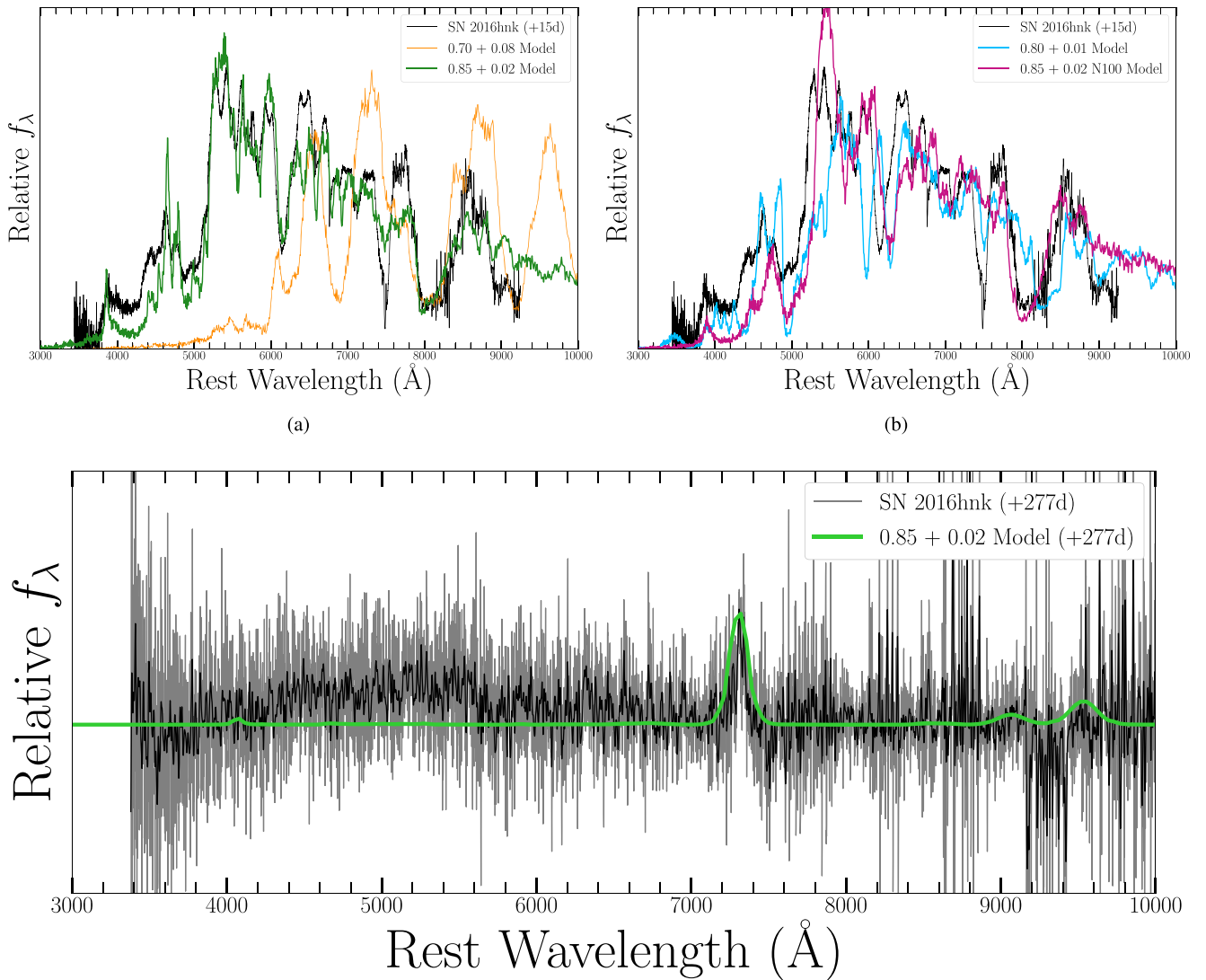
Figure 17. (a)/(b) Early-time model comparison of SN 2016hnk (black) and double detonations of $0.70-0.85\ M_\odot$ WDs with $0.01-0.08\ M_\odot$ helium shells. The best-fitting, non-mixed $0.85 + 0.02$ model is shown in forest green. Only the $0.80 + 0.02$ N100 model spectrum (shown in violet–red) contains mixing of ejecta. Models presented are from Polin et al. (2019a). Phases presented are with respect to explosion. (c) Nebular comparison of SN 2016hnk and best-fitting $0.85 + 0.02$ helium shell nebular model from Polin et al. (2019b). Phases are also with respect to estimated explosion date.

than SN 2016hnk ($0.91\ M_\odot$ versus $0.82\ M_\odot$), and may take longer to become optically thin. An LTE condition is not applicable once the ejecta beings to become optically thin, which typically occurs ∼30 days after explosion for sub-Chandrasekhar mass ejecta (light blue shaded region in Figure 16). A more detailed treatment of non-LTE conditions could explain the slower light-curve decline in SN 2016hnk. Furthermore, our 1D helium shell model does not account for additional physics such as asymmetries or external emission components that could have influenced the increased light-curve flux relative to the models. Nonetheless, while the model is an approximation of the SN explosion physics, it provides a reasonable match to the observables with only two free parameters (the mass of the helium shell and the mass of the underlying WD).

In Figure 16(c) we compare $g - r$ and $r - i$ colors of SN 2016hnk to various helium shell models from Polin et al. (2019a). Overall both mixed and unmixed models have bluer colors than those observed in SN 2016hnk. However, in the LTE regime the models are consistent to within 0.3 mag of

SN 2016hnk's $g - r$ and $r - i$ color evolution. We cannot constrain the helium shell scenario further given the lack of pre-maximum color information.

As shown in Figure 17(a), the photospheric spectra of SN 2016hnk are best reproduced by a detonation model involving a $0.85\ M_\odot$ WD and $0.02\ M_\odot$ helium shell. This model has a total synthesized nickel yield of $0.045\ M_\odot$. For reference, we compare SN 2016hnk to other model spectra from Polin et al. (2019a) with varying WD and shell masses in Figures 17(a)/(b). We track the evolution of the best-fitting models with respect to observations in a spectral time series presented in Figure 18(a). We include additional spectral data from G19 in order to present comparisons from +15 days out to +33 days after explosion, the final phase being the time when the LTE model assumption becomes unreliable. In Figure 18(b) we present Si II and Ca II velocities for SNe 2005ke, 2016hnk, and 2018byg with respect to the same line velocities from the best-fitting helium shell model. In both figures we demonstrate a time-dependent consistency between the complete spectral profile, as well as individual ion

(a)
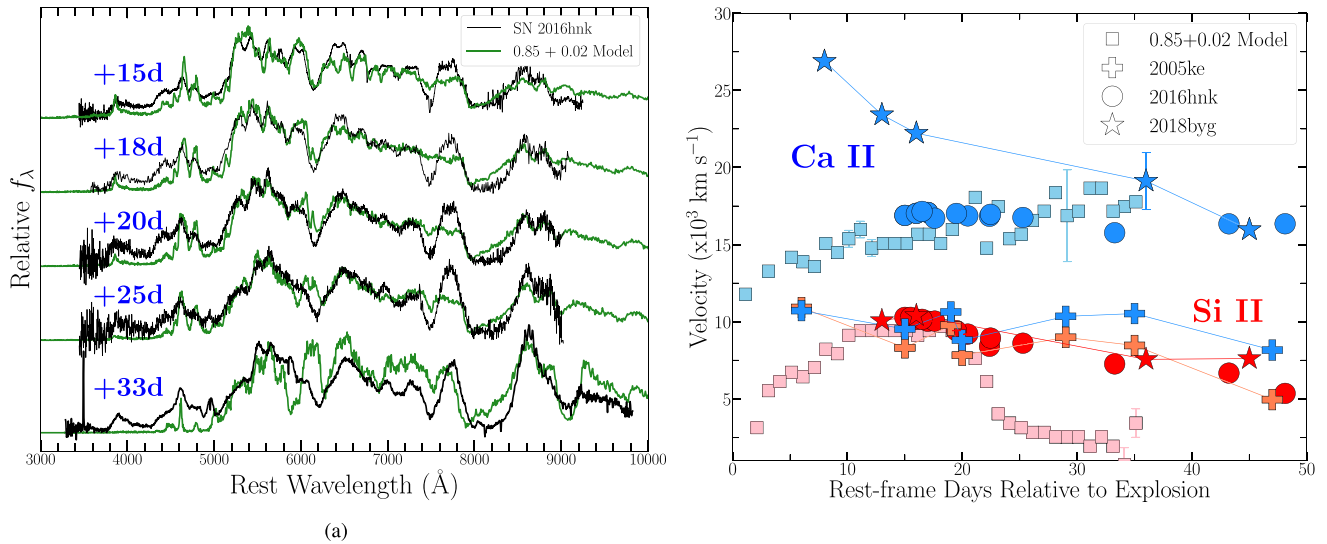
Figure 18. (a) Spectral time series of SN 2016hnk (black) and the best-fitting helium shell detonation model (green) with phases relative to explosion. Spectral models are only shown out to ~30 days, which is where the local thermal equilibrium approximation breaks down and the modeling becomes less reliable. These additional data not shown in Figure 3 are taken from G19. (b) Evolution of Ca II and Si II velocities, calculated from fitted absorption minima, for SNe 2005ke (plus signs), 2016hnk (circles), and 2018byg (stars) with respect to those derived from best-fitting model spectra (squares).

velocities, observed in SN 2016hnk and the 0.85 $M_\odot$ WD plus 0.02 $M_\odot$ helium shell model.

Using the nebular companion to Sedona, SedoNeb (Botyánszki & Kasen 2017), we are able to examine our best-fitting 0.85+0.02 $M_\odot$ model in the nebular phase following the methods outlined in Polin et al. (2019b), who investigated the nebular features of double detonations and showed that low-mass scenarios would appear Ca-rich in the nebular phase. These methods require the SN ejecta to be fully optically thin in the desired wavelengths in order to produce a nebular spectrum. In this way we are able to examine the observational signatures of our model in the nebular phase (beginning ~150 days after explosion). The resulting spectrum is shown in Figure 17(c) as a green line. This model is consistent with the nebular spectrum of SN 2016hnk at +277 days after explosion, with [Ca II] emission being the dominant feature in both the simulation and observation. This is the first potential thick helium shell double-detonation that we are able to compare to the models in both epochs as the nebular spectrum of SN 2018byg could not be obtained.

The thickness of the helium shell in our preferred double-detonation model (~0.02 $M_\odot$) suggests an explosion scenario involving a larger, non-degenerate companion to the C/O WD. A progenitor system that works well with this detonation mechanism is a He or sdB star + C/O WD binary system, wherein the WD is accreting He-rich material from the non-degenerate companion. Such a configuration has been explored in simulations for both steady and time-varying dynamical accretion scenarios involving a 0.4–0.6 $M_\odot$ He or sdB donor star (Nomoto 1982a; Woosley et al. 1989; Woosley & Kasen 2011). Recent modeling has demonstrated that significant build-up of a thick helium layer on the WD surface, combined with proper treatment of nuclear reaction networks (e.g., CNO or NCO burning), can trigger a shell detonation (Shen & Bildsten 2014; Shen & Moore 2014; Brooks et al. 2015; Bauer et al. 2017). Consequently, De et al. (2019) discuss how SN 2018byg is consistent with a 0.48 $M_\odot$ sdB star model presented by Bauer et al. (2017) wherein dynamical

accretion led to a large helium envelope (>0.1 $M_\odot$) on the sub-Chandrasekhar C/O WD surface, eventually resulting in a shell detonation. While our models do not consider the pre-cursor accretion process to the double-detonation, the success of sdB + C/O WD binary configurations in achieving a helium envelope detonation makes these accretion scenarios viable candidates for producing the thick helium shells present within our models.

6. Discussion

6.1. Reddening

The observed color evolution shows that SN 2016hnk is a highly reddened object. Currently, there is an established link between dust reddening and the strength of Na I D absorption for Milky Way stars and extragalactic SNe (Phillips et al. 2013). The lack of Na I D absorption in SN 2016hnk is a strong indication that the SN is unaffected by host reddening and that its red colors are intrinsic to the explosion. We further demonstrate this fact by de-reddening SN 2016hnk's color evolution. As shown in Figure 7(a), we de-redden $B - V$ colors to match the bluest SNe Ia. Assuming a Fitzpatrick (1999) reddening law, this corresponds to an $E(B - V) = 0.45$ mag, which is the same as the host galaxy extinction reported in G19. While this shift does make the $g - r$ colors more consistent with other objects, de-reddening the SN 2016hnk photometry causes the $r - i$ color evolution to be even more inconsistent with SNe Ia. Therefore, if SN 2016hnk has a host-galaxy reddening of $E(B - V) = 0.45$ mag, then it would be $\geqslant 0.20$ mag intrinsically bluer than all other SNe Ia, including those similar to SN 1991bg, in $r - i$. While possible, this scenario requires both a relatively large dust reddening with no Na D absorption, in contrast to other SNe with similar reddening, and intrinsically peculiar colors. Our preferred scenario of minimal reddening and intrinsically peculiar colors requires less exceptional circumstances. Furthermore, a single-explosion model can explain the peculiar colors, luminosity, and spectral evolution of SN 2016hnk.

SN 2016hnk's red colors can be explained by the helium shell double-detonation model proposed for this object. As shown in Section 5, the detonation of a helium shell on the surface of a C/O WD will pollute the outer layers of ejecta with Fe-group elements, which will suppress blueward flux. The products of the helium shell detonation will produce ashes that will cause the SN to have redder colors throughout its evolution, as observed in SN 2016hnk. Thus we attribute the observed red colors of SN 2016hnk to a helium shell detonation, which we show to be consistent with observations of this event in Figures 16 and 17.

6.2. Modeling Approach

The challenge in modeling SN 2016hnk lies in the lack of early-time data. The typical approach is to constrain the model parameters solely with photometry. The magnitude of the early flux excess constrains the mass of the helium shell, and peak magnitude reflects the total mass of the progenitor star. We would then compare the spectra and see if the event is consistent with a double-detonation explosion. This method was used for SN 2018byg by De et al. (2019). However, in the case of 2016hnk, we can only constrain the total mass (or equivalently a ^{56}Ni mass) from the peak luminosity, and we estimate the mass of the helium shell by examining the synthetic spectra at the time of peak brightness. When we examine the line-blanketed part of the spectrum ($\lambda < 5000\,\text{Å}$) we find a good agreement with the $0.02\,M_\odot$ helium shell.

Another source of possible concern is the poor fit of our model to the slow decline of 2016hnk (Figure 16). This might be the result of the LTE approximation in the radiative transport calculations, which underpredict the flux once the ejecta becomes optically thin. This occurs $\sim$30–40 days after explosion for sub-Chandrasekhar mass models. Future non-LTE modeling is required to understand if the slow decline of SN 2016hnk can be modeled with a double-detonation explosion of this total mass of $0.87\,M_\odot$ or if the slow decline requires a more massive ejecta to account for the required diffusion time as, suggested in G19. However, an alternative explanation for this light-curve plateau is the emergence of blueward flux that was previous suppressed by Fe-group elements in the outer ejecta. This would occur once the outer ejecta expands and becomes optically thin, thus causing an increase in flux in the bands affected by early-time line blanketing (e.g., u, B, g, V bands). This scenario seems plausible based on the spectral evolution after $t \sim 20$ days in both our data set and in G19, but a more robust analysis of spectral color evolution would need to be done to verify this model.

6.3. Comparison to G19

Our observational inferences on SN 2016hnk are similar to those presented in G19. We both find SN 2016hnk to be a peculiar thermonuclear object with a low overall luminosity and observed red colors. We obtain similar values for $\Delta m_{15}(B)$ and M_B at peak, both of which are dissimilar from those found in SNe Ia sub-classes. Additionally, both of our observations have shown SN 2016hnk to be rich in high-velocity calcium, which dominates the nebular spectrum as [Ca II] emission. We furthermore agree that exotic elements such as Sc II, Cr II, and Sr II are most likely not found within the SN 2016hnk photospheric spectra. Despite its spectral similarity to

PTF09dav, we find that blueward line profiles can be effectively modeled with Fe, Co, and Ti ions, similar to those found in G19. We also acknowledge the similarities between SN 2016hnk and 91bg-like peak spectra, as shown in G19. The closest matching spectral features are in the 5000–6300 Å wavelength range, which includes similar Si II absorption profiles in both objects (Figure 11(a)).

However, additional observations and modeling presented in this paper lead to a different overall interpretation than G19 on the intrinsic nature of SN 2016hnk. The observed rise time and velocities, in addition to consistency with shell models, demonstrate that SN 2016hnk produced $0.9\,M_\odot$ of ejecta, thus making it a sub-Chandrasekhar mass explosion. This SN was extremely Fe-poor, as shown by its low total Ni-mass and lack of Fe-group ions in its nebular spectra (Sections 3.2 and 4.2). As discussed in Section 6.1, the highly reddened colors are intrinsic to SNe and require an explosion mechanism to suppress blueward flux as shown in photospheric spectra. Consequently, we attribute these observed characteristics to a helium shell double-detonation of a sub-Chandrasekhar mass C/O WD.

In this paper we have demonstrated the physical differences between SN 2016hnk and 91bg-like objects. First, SN 2016hnk produced a small amount of Fe-group elements relative to 91bg-like events. This is demonstrated by the low inferred Ni-mass and lack of visible Fe-group elements in late-time spectra. Furthermore, as illustrated in Figure 5, SN 2016hnk has very different M_B versus $\Delta m_{15}(B)$ measurement relative to 91bg-like events. The intrinsic color evolution of SN 2016hnk is also unlike any sub-luminous SN Ia; the SN's highly reddened $B - V$ colors, in addition to "bluer" $r - i$, are inconsistent with other events (Figure 7). Additionally, the barred spiral host galaxy of SN 2016hnk may indicate a distinct stellar progenitor system from 91bg-like objects, which are typically found in elliptical galaxies with older stellar populations (van den Bergh et al. 2005; however, see Höflich et al. 2002; Garnavich et al. 2004). Conversely, if SN 2016hnk does in fact belong to the 91bg-like sub-class, it is the most extreme example yet observed.

6.4. Classification and Origins

The properties of SN 2016hnk challenge the traditional classification schemes of both sub-luminous SNe Ia and Ca-rich transients. Upon discovery, SN 2016hnk was classified as a 91bg-like object because of its spectral features and low luminosity. However, its prominent Ca II features and "gap" absolute magnitude placed the SN in Ca-rich class. Its spectroscopic similarity to PTF09dav around maximum light also made the Ca-rich classification plausible. The Ca-rich distinction was later confirmed by its pre-nebular and nebular spectra, which were dominated by [Ca II] emission in addition to having an integrated [Ca II]/[O I] flux ratio greater than 2.

The ambiguity of SN 2016hnk's classification points to a need for diligence in understanding the similarities between low-luminosity thermonuclear objects. While it is true that SN 2016hnk shows some spectroscopic similarities to 91bg-like objects near peak, there are prominent physical differences that set these objects apart. Like Ca-rich events, SN 2016hnk was significantly more Fe-poor than any 91bg-like object yet observed. This became most apparent in nebular spectra and may be an indication that some 91bg-like or sub-luminous SNe Ia are mis-classified. There could be a number of sub-

luminous SN Ia that are classified as such using maximum light spectra, but more physically resemble a "16hnk-like" or Ca-rich event. This is further supported by the limited number of sub-luminous objects that are tracked out to nebular times.

The color evolution of SN 2016hnk was essential in determining physical distinctions between the SN and sub-luminous SNe Ia. We emphasize the need for multi-band color information in order to understand how highly reddened, 16hnk-like SNe might compare to the larger thermonuclear sample. Furthermore, high-cadence color evolution could help to identify more than examples of thin shell detonations of sub-Chandrasekhar mass WDs.

As shown in De et al. (2019), SN 2018byg was thought to be a relatively rare event. Due to the observational similarity and consistent explosion models between both objects, we may initially conclude that SN 2016hnk was also a rare event with respect to thermonuclear SNe. This indicates that there are physical distinctions between the helium shell detonations that can explain SNe 2016hnk and 2018byg, in addition to models that have been shown to reproduce normal and sub-luminous SNe Ia (e.g., Shen et al. 2018; Polin et al. 2019a; Townsley et al. 2019). The thin shell detonation models that best matched these two SNe were distinct in their production of suppressed blueward flux, Fe-group line blanketing, high ($>18,000 \, \mathrm{km \, s^{-1}}$) Ca II velocities, and an intrinsically red color evolution. These physical properties can thus be applied as tracers for identifying more events like the apparent helium shell detonations that well explain SNe 2016hnk and 2018byg.

Furthermore, it may be possible that many Ca-rich events are caused by variations on the helium shell double-detonation model. A similar model was invoked to explain SN 2005E and it may be the case that other Ca-rich events could now be explained with new varieties of helium shell detonations. These events have noticeable similarities to this model such as low luminosities, reddened colors, dominant [Ca II] emission at nebular times, and rapidly evolving light curves. Additionally, iPTF16hgs has a double-peaked light curve, which may be matched to the first ^{48}Cr peak produced in helium shell models. However, this explosion scenario needs to explain the He I observations in many Ca-rich objects; such an observation may require a fine-tuning of helium detonation on the WD surface in order to allow for sufficient amounts of un-burned helium to remain in the SN ejecta. Nonetheless, the observed Hα emission in PTF09dav poses a serious problem for this model since no hydrogen is produced in such an explosion.

7. Conclusion

In this paper we have presented observations and modeling of the Ca-rich transient SN 2016hnk. We summarize our primary observational findings below.

1. SN 2016hnk is intrinsically red compared to other thermonuclear objects. This is demonstrated by the lack of Na D absorption in photospheric spectra and the even "bluer" $r - i$ color evolution if any "de-reddening" is applied.
2. Photospheric spectra show strong, high-velocity Ca II features ($\approx -18,000 \, \mathrm{km \, s^{-1}}$) and suppressed blueward flux from line blanketing of Fe-group elements.
3. Nebular spectra are O- and Fe-poor, with the most prominent feature being [Ca II] emission.

4. SN 2016hnk has a rise time of $t_r = 15 \pm 2$ days and a slow, "plateau" decline in B-band relative to SNe Ia.
5. Peak absolute magnitude of $M_B = -15.40 \pm 0.088$ mag and decline parameter of $\Delta m_{15}(B) = 1.31 \pm 0.085$ mag.
6. Total nickel and ejecta masses are $M_{\mathrm{Ni}} = 0.03 \pm 0.01$ and $M_{\mathrm{ej}} = 0.9 \pm 0.3 \, M_\odot$, respectively.

SN 2016hnk is most similar to SN 2018byg, a thermonuclear SN that is observationally consistent with a helium shell detonation on the surface of a sub-Chandrasekhar mass C/O WD. In their peak spectra, SNe 2016hnk and 2018byg both have high-velocity Ca II absorption features and significant line blanketing among Fe-group elements. Both objects are instrinically reddened and have consistent $g - r$ and $r - i$ color evolution to within 0.5mag. While the light-curve evolution of both objects is similar, SN 2016hnk has a faster rise time and a somewhat slower decline in r and i bands.

Given these physical similarities between both objects, we compare SN 2016hnk observations to observables produced in thin helium shell detonations on sub-Chandrasekhar mass WDs. Using the models of Polin et al. (2019a), we find SN 2016hnk to be consistent with the detonation of a $0.85 \, M_\odot$ WD with a $0.02 \, M_\odot$ helium shell. This model is well-matched to photospheric and nebular spectra, but cannot fully reproduce the slow declining light-curve evolution observed in SN 2016hnk at $t > 30$ days post-explosion. However, we attribute this discrepancy to LTE assumptions which break down as the SN becomes optically thin at >20 days after peak luminosity. Nonetheless, the ashes from such a helium detonation can effectively explain the red colors of SN 2016hnk. Furthermore, the increased Fe-group elements produced in the outer ejecta by this type of explosion can reproduce the observed Fe-group line blanketing and suppressed blueward flux in SN 2016hnk's photospheric spectra.

Finally, we have determined multiple observational differences between SN 2016hnk and 91bg-like SNe. First, SN 2016hnk is highly reddened compared to all normal and sub-luminous SNe Ia. De-reddening SN 2016hnk's $B - V$ colors to match those of SNe Ia results in an even more substanial difference between these obejcts in $r - i$. Additionally, SN 2016hnk has a lower peak M_B and smaller $\Delta m_{15}(B)$ than typical 91bg-like events. Lastly, SN 2016hnk is Fe-poor relative to all 91bg-like objects; SN 2016hnk has no nebular spectral signatures of forbidden Fe, Co, or Ni lines and its total inferred Ni-mass is lower than all known sub-luminous SNe Ia. These stark differences may indicate that SN 2016hnk is the most extreme example of a sub-luminous SNe Ia to date.

Appendix

In this section we present data tables for all photometric and spectroscopic observations of SN 2016hnk (Tables A1-A2).

Table A1
Optical Photometry of SN 2016hnk

MJD	Phase[a]	Filter	Magnitude	Uncertainty	Instrument
57693.31	+3.11	u	21.16	0.13	Swope
57693.29	+3.09	B	19.11	0.08	Swope
57693.30	+3.10	B	19.11	0.03	Swope
57695.26	+5.06	B	19.24	0.07	Swope
57695.26	+5.06	B	19.27	0.02	Swope
57713.30	+23.10	B	20.51	0.13	Swope
57719.24	+29.04	B	20.63	0.06	Swope
57721.18	+30.98	B	20.65	0.05	Swope
57693.30	+3.10	V	17.63	0.02	Swope
57695.27	+5.07	V	17.66	0.02	Swope
57713.30	+23.10	V	18.86	0.06	Swope
57719.25	+29.05	V	19.16	0.04	Swope
57721.18	+30.98	V	19.25	0.03	Swope
57693.32	+3.12	g	18.36	0.02	Swope
57695.28	+5.08	g	18.45	0.02	Swope
57695.28	+5.08	g	18.89	0.02	Swope
57713.28	+23.08	g	19.90	0.07	Swope
57719.26	+29.06	g	20.09	0.04	Swope
57721.17	+30.97	g	20.12	0.04	Swope
57746.20	+56.00	g	20.33	0.04	Swope
57751.15	+60.95	g	20.35	0.04	Swope
57752.17	+61.97	g	20.38	0.03	Swope
57754.17	+63.97	g	20.42	0.04	Swope
57774.11	+83.91	g	20.82	0.08	Swope
57778.12	+87.92	g	20.55	0.08	Swope
57780.09	+89.89	g	20.75	0.12	Swope
57785.07	+94.87	g	20.91	0.08	Swope
57801.04	+110.84	g	21.05	0.09	Swope
57804.02	+113.82	g	20.97	0.12	Swope
57693.32	+3.12	r	17.23	0.01	Swope
57713.28	+23.08	r	18.32	0.06	Swope
57713.28	+23.08	r	18.29	0.03	Swope
57719.26	+29.06	r	18.46	0.02	Swope
57719.22	+29.02	r	18.59	0.05	Swope
57721.16	+30.96	r	18.42	0.06	Swope
57721.16	+30.96	r	18.45	0.02	Swope
57744.20	+54.00	r	19.24	0.06	Swope
57746.19	+55.99	r	19.37	0.12	Swope
57746.19	+55.99	r	19.26	0.03	Swope
57751.14	+60.94	r	19.47	0.03	Swope
57752.15	+61.95	r	19.48	0.09	Swope
57752.15	+61.95	r	19.43	0.02	Swope
57754.16	+63.96	r	19.72	0.15	Swope
57754.16	+63.96	r	19.56	0.03	Swope
57774.10	+83.90	r	20.19	0.06	Swope
57778.11	+87.91	r	20.23	0.09	Swope
57780.10	+89.90	r	20.42	0.11	Swope
57785.08	+94.88	r	20.67	0.08	Swope
57801.03	+110.83	r	21.00	0.12	Swope
57693.32	+3.12	i	17.47	0.02	Swope
57695.28	+5.08	i	17.50	0.01	Swope
57713.28	+23.08	i	18.19	0.03	Swope
57719.26	+29.06	i	18.39	0.03	Swope
57721.17	+30.97	i	18.50	0.02	Swope
57744.20	+54.00	i	19.35	0.09	Swope
57746.19	+55.99	i	19.30	0.04	Swope
57751.14	+60.94	i	19.46	0.04	Swope
57752.16	+61.96	i	19.45	0.03	Swope
57754.17	+63.97	i	19.44	0.04	Swope
57774.11	+83.91	i	19.80	0.07	Swope
57778.12	+87.94	i	19.93	0.09	Swope
57785.08	+94.88	i	20.14	0.08	Swope
57780.09	+89.89	i	20.01	0.14	Swope

Table A1
(Continued)

MJD	Phase[a]	Filter	Magnitude	Uncertainty	Instrument
57801.04	+110.84	i	20.18	0.09	Swope
57804.02	+113.82	i	20.02	0.15	Swope
57690.20	+0.00	B	18.99	0.07	LCOGT
57690.81	+0.61	B	19.00	0.09	LCOGT
57690.82	+0.62	B	19.01	0.09	LCOGT
57692.83	+2.63	B	19.04	0.04	LCOGT
57694.92	+4.72	B	19.18	0.04	LCOGT
57695.09	+4.89	B	19.29	0.02	LCOGT
57697.43	+7.23	B	19.55	0.06	LCOGT
57698.91	+8.71	B	19.75	0.06	LCOGT
57699.00	+8.80	B	19.83	0.06	LCOGT
57701.27	+11.07	B	19.99	0.07	LCOGT
57701.62	+11.42	B	20.05	0.09	LCOGT
57702.58	+12.38	B	20.17	0.14	LCOGT
57707.82	+17.62	B	20.40	0.05	LCOGT
57711.25	+21.05	B	20.46	0.25	LCOGT
57711.87	+21.67	B	20.47	0.08	LCOGT
57713.16	+22.96	B	20.52	0.11	LCOGT
57714.51	+24.31	B	20.53	0.09	LCOGT
57717.17	+26.97	B	20.58	0.07	LCOGT
57717.85	+27.65	B	20.59	0.08	LCOGT
57721.06	+30.86	B	20.58	0.08	LCOGT
57721.81	+31.61	B	20.62	0.09	LCOGT
57726.84	+36.64	B	20.69	0.02	LCOGT
57733.90	+43.70	B	20.80	0.05	LCOGT
57736.91	+46.71	B	20.81	0.26	LCOGT
57741.15	+50.95	B	20.83	0.07	LCOGT
57745.04	+54.84	B	20.89	0.09	LCOGT
57746.18	+55.98	B	20.93	0.09	LCOGT
57747.01	+56.81	B	20.94	0.09	LCOGT
57752.87	+62.67	B	21.01	0.11	LCOGT
57755.72	+65.52	B	20.95	0.10	LCOGT
57757.11	+66.91	B	20.99	0.16	LCOGT
57689.93	−0.27	V	17.65	0.03	LCOGT
57690.82	+0.62	V	17.67	0.05	LCOGT
57692.83	+2.63	V	17.63	0.03	LCOGT
57695.10	+4.90	V	17.78	0.02	LCOGT
57697.44	+7.24	V	17.90	0.03	LCOGT
57698.92	+8.72	V	17.93	0.03	LCOGT
57701.27	+11.07	V	18.21	0.04	LCOGT
57701.63	+11.43	V	18.27	0.03	LCOGT
57702.58	+12.38	V	18.33	0.07	LCOGT
57707.07	+16.87	V	18.60	0.21	LCOGT
57707.82	+17.62	V	18.65	0.06	LCOGT
57708.63	+18.43	V	18.70	0.14	LCOGT
57711.87	+21.67	V	18.69	0.05	LCOGT
57713.16	+22.96	V	18.84	0.07	LCOGT
57714.51	+24.31	V	18.94	0.08	LCOGT
57717.18	+26.98	V	19.07	0.07	LCOGT
57717.85	+27.65	V	19.10	0.05	LCOGT
57721.07	+30.87	V	19.26	0.06	LCOGT
57721.82	+31.62	V	19.26	0.07	LCOGT
57726.85	+36.65	V	19.34	0.09	LCOGT
57733.89	+43.69	V	19.51	0.20	LCOGT
57736.92	+46.72	V	19.52	0.11	LCOGT
57745.05	+54.85	V	19.56	0.09	LCOGT
57746.19	+55.99	V	19.57	0.08	LCOGT
57747.02	+56.82	V	19.63	0.08	LCOGT
57752.88	+62.68	V	19.75	0.10	LCOGT
57755.73	+65.53	V	19.80	0.09	LCOGT
57761.50	+71.30	V	19.94	0.16	LCOGT
57695.28	+5.08	g	18.58	0.01	LCOGT
57699.00	+8.80	g	19.26	0.03	LCOGT
57701.63	+11.43	g	19.32	0.04	LCOGT

Table A1
(Continued)

MJD	Phase[a]	Filter	Magnitude	Uncertainty	Instrument
57706.89	+16.69	g	19.57	0.08	LCOGT
57707.82	+17.62	g	19.62	0.08	LCOGT
57711.88	+21.68	g	19.75	0.04	LCOGT
57717.86	+27.66	g	20.01	0.04	LCOGT
57721.07	+30.87	g	20.07	0.04	LCOGT
57721.82	+31.62	g	20.07	0.04	LCOGT
57726.84	+36.64	g	20.17	0.08	LCOGT
57728.10	+37.90	g	20.18	0.05	LCOGT
57729.59	+39.39	g	20.19	0.12	LCOGT
57733.88	+43.68	g	20.25	0.06	LCOGT
57741.17	+50.97	g	20.25	0.05	LCOGT
57745.17	+54.97	g	20.28	0.06	LCOGT
57747.16	+56.96	g	20.32	0.04	LCOGT
57752.87	+62.67	g	20.40	0.05	LCOGT
57761.22	+71.02	g	20.47	0.08	LCOGT
57690.82	+0.62	r	17.30	0.02	LCOGT
57690.81	+0.61	r	17.30	0.03	LCOGT
57692.83	+2.63	r	17.28	0.02	LCOGT
57694.93	+4.73	r	17.24	0.04	LCOGT
57695.27	+5.07	r	17.26	0.04	LCOGT
57697.44	+7.24	r	17.34	0.02	LCOGT
57698.93	+8.73	r	17.37	0.01	LCOGT
57699.10	+8.90	r	17.54	0.04	LCOGT
57700.89	+10.69	r	17.62	0.12	LCOGT
57701.27	+11.07	r	17.65	0.05	LCOGT
57702.58	+12.38	r	17.75	0.04	LCOGT
57703.23	+13.03	r	17.80	0.14	LCOGT
57704.31	+14.11	r	17.90	0.10	LCOGT
57706.92	+16.72	r	17.99	0.12	LCOGT
57707.31	+17.11	r	17.99	0.14	LCOGT
57708.63	+18.43	r	18.05	0.08	LCOGT
57709.87	+19.67	r	18.10	0.06	LCOGT
57710.18	+19.98	r	18.16	0.11	LCOGT
57711.88	+21.68	r	18.14	0.02	LCOGT
57712.85	+22.65	r	18.29	0.03	LCOGT
57713.18	+22.98	r	18.27	0.06	LCOGT
57714.51	+24.31	r	18.36	0.04	LCOGT
57717.18	+26.98	r	18.42	0.03	LCOGT
57717.86	+27.66	r	18.42	0.02	LCOGT
57721.82	+31.62	r	18.49	0.03	LCOGT
57722.22	+32.02	r	18.54	0.15	LCOGT
57726.83	+36.63	r	18.60	0.12	LCOGT
57728.10	+37.90	r	18.69	0.09	LCOGT
57729.55	+39.35	r	18.71	0.11	LCOGT
57733.90	+43.71	r	18.80	0.08	LCOGT
57736.94	+46.74	r	18.87	0.10	LCOGT
57741.21	+51.01	r	18.92	0.06	LCOGT
57745.21	+55.01	r	19.03	0.11	LCOGT
57747.12	+56.92	r	19.11	0.08	LCOGT
57752.87	+62.67	r	19.29	0.04	LCOGT
57761.13	+70.93	r	19.50	0.20	LCOGT
57762.86	+72.66	r	19.54	0.16	LCOGT
57690.82	+0.62	i	17.42	0.04	LCOGT
57690.20	+0.00	i	17.48	0.03	LCOGT
57692.83	+2.63	i	17.46	0.04	LCOGT
57694.82	+4.62	i	17.46	0.04	LCOGT
57695.29	+5.09	i	17.49	0.03	LCOGT
57695.28	+5.08	i	17.50	0.04	LCOGT
57695.04	+4.84	i	17.52	0.05	LCOGT
57698.76	+8.56	i	17.55	0.05	LCOGT
57699.01	+8.81	i	17.60	0.06	LCOGT
57700.20	+10.00	i	17.75	0.12	LCOGT
57701.64	+11.44	i	17.85	0.09	LCOGT
57701.27	+11.07	i	17.89	0.04	LCOGT

Table A1
(Continued)

MJD	Phase[a]	Filter	Magnitude	Uncertainty	Instrument
57702.58	+12.38	i	17.92	0.05	LCOGT
57704.33	+14.13	i	17.93	0.10	LCOGT
57706.90	+16.70	i	17.96	0.09	LCOGT
57707.29	+17.09	i	18.08	0.08	LCOGT
57707.83	+17.63	i	18.08	0.08	LCOGT
57707.83	+17.63	i	18.11	0.08	LCOGT
57708.63	+18.43	i	18.16	0.09	LCOGT
57710.85	+20.65	i	18.23	0.02	LCOGT
57711.89	+21.69	i	18.28	0.07	LCOGT
57711.26	+21.06	i	18.32	0.10	LCOGT
57713.16	+22.96	i	18.39	0.06	LCOGT
57715.20	+25.00	i	18.45	0.10	LCOGT
57717.87	+27.67	i	18.46	0.07	LCOGT
57721.83	+31.63	i	18.48	0.09	LCOGT
57722.20	+32.00	i	18.59	0.15	LCOGT
57726.87	+36.67	i	18.72	0.12	LCOGT
57728.12	+37.92	i	18.75	0.08	LCOGT
57733.90	+43.70	i	18.81	0.14	LCOGT
57736.91	+46.71	i	18.93	0.10	LCOGT
57741.19	+50.99	i	19.11	0.10	LCOGT
57745.19	+54.99	i	19.18	0.13	LCOGT
57747.18	+56.98	i	19.27	0.13	LCOGT
57752.88	+62.68	i	19.40	0.17	LCOGT
57761.12	+70.92	i	19.66	0.15	LCOGT
57762.89	+72.69	i	19.71	0.12	LCOGT
57696.97	+6.77	z	17.26	0.06	LCOGT
57701.79	+11.59	z	17.71	0.19	LCOGT
57710.26	+20.06	z	17.74	0.07	LCOGT
57711.79	+21.59	z	17.68	0.11	LCOGT
57720.82	+30.62	z	17.87	0.21	LCOGT
57726.82	+36.62	z	17.81	0.17	LCOGT
57736.95	+46.75	z	18.15	0.27	LCOGT
57741.20	+51.00	z	18.65	0.16	LCOGT
57690.40	+0.20	g	18.15	0.02	PS1
57697.40	+7.20	g	18.51	0.04	PS1
57709.38	+19.18	g	19.48	0.13	PS1
57736.31	+46.11	g	19.77	0.14	PS1
57744.27	+54.07	g	20.01	0.13	PS1
57690.40	+0.20	r	17.29	0.01	PS1
57697.40	+7.20	r	17.31	0.01	PS1
57709.38	+19.18	r	18.11	0.03	PS1
57736.31	+46.11	r	18.98	0.05	PS1
57744.27	+54.07	r	19.23	0.05	PS1
57690.40	+0.20	i	17.40	0.01	PS1
57697.40	+7.20	i	17.44	0.02	PS1
57709.39	+19.19	i	18.10	0.03	PS1
57736.31	+46.11	i	18.85	0.05	PS1
57744.27	+54.07	i	19.26	0.07	PS1
57765.23	+75.03	i	19.61	0.06	PS1
57765.24	+75.04	i	19.72	0.07	PS1
57765.26	+75.06	i	19.74	0.06	PS1
57765.27	+75.07	i	19.75	0.06	PS1
57709.39	+19.19	z	17.68	0.03	PS1
57736.31	+46.11	z	18.28	0.04	PS1
57744.27	+54.07	z	18.57	0.05	PS1
57671.55	−18.65	orange	>20.20	⋯	ATLAS
57680.53	−9.67	orange	18.90	0.34	ATLAS
57700.46	+10.26	orange	17.61	0.08	ATLAS
57704.44	+14.24	orange	17.82	0.20	ATLAS
57712.46	+22.26	orange	17.99	0.25	ATLAS
57736.36	+46.16	orange	18.55	0.31	ATLAS
57743.36	+53.16	orange	18.63	0.19	ATLAS
57659.57	−30.63	cyan	>21.79	⋯	ATLAS
57663.56	−26.64	cyan	>21.70	⋯	ATLAS

Jacobson-Galán et al.

Table A1
(Continued)

MJD	Phase[a]	Filter	Magnitude	Uncertainty	Instrument
57667.56	−22.64	cyan	>20.32	⋯	ATLAS
57688.51	−1.69	cyan	17.80	0.07	ATLAS
57696.46	+6.26	cyan	17.83	0.06	ATLAS
57716.43	+26.23	cyan	18.67	0.17	ATLAS
57744.34	+54.14	cyan	19.72	0.33	ATLAS
57756.34	+66.14	cyan	20.01	0.41	ATLAS
57954.56	+264.36	B	>23.40	⋯	Keck
57981.54	+291.34	B	>23.40	⋯	Keck
57981.51	+291.31	V	>23.50	⋯	Keck
57954.57	+264.37	R	>23.30	⋯	Keck
57981.54	+291.34	R	>23.40	⋯	Keck
57981.51	+291.31	I	23.57	0.09	Keck

Note.
[a] Relative to B maximum (MJD 57690.18).

(This table is available in machine-readable form.)

Table A2
Optical Spectroscopy of SN 2016hnk

MJD	Phase[a]	Telescope	Instrument	Wavelength Range
57691	+1	SOAR	Goodman	3000–9000 Å
57692	+2	SALT	RSS	3000–9000 Å
57693	+3	NOT	ALFOSC	3000–9000 Å
57694	+4	NOT	ALFOSC	3000–9000 Å
57722	+32	Mayall	KOSMOS	3000–9000 Å
57749	+59	Mayall	KOSMOS	3000–9000 Å
57756	+66	SOAR	Goodman	3000–9000 Å
57954	+264	Keck I	LRIS	3000–9000 Å

Note.
[a] Relative to B maximum (MJD 57690.18).

ORCID iDs

Wynn V. Jacobson-Galán ⬤ https://orcid.org/0000-0003-1103-3409
Georgios Dimitriadis ⬤ https://orcid.org/0000-0001-9494-179X
Charles D. Kilpatrick ⬤ https://orcid.org/0000-0002-5740-7747
Raffaella Margutti ⬤ https://orcid.org/0000-0003-4768-7586
David A. Coulter ⬤ https://orcid.org/0000-0003-4263-2228
Saurabh W. Jha ⬤ https://orcid.org/0000-0001-8738-6011
David O. Jones ⬤ https://orcid.org/0000-0002-6230-0151
Yen-Chen Pan ⬤ https://orcid.org/0000-0001-8415-6720
Anthony L. Piro ⬤ https://orcid.org/0000-0001-6806-0673

References

Alam, S., Albareti, F. D., Allende Prieto, C., et al. 2015, ApJS, 219, 12
Almgren, A. S., Beckner, V. E., Bell, J. B., et al. 2010, ApJ, 715, 1221
Arnett, W. D. 1982, ApJ, 253, 785
Bauer, E. B., Schwab, J., & Bildsten, L. 2017, ApJ, 845, 97
Becker, A. 2015, HOTPANTS: High Order Transform of PSF ANd Template Subtraction, v 5.1.10b, Astrophysics Source Code Library, ascl:1504.004
Bildsten, L., Shen, K. J., Weinberg, N. N., & Nelemans, G. 2007, ApJL, 662, L95
Bilir, S., Karaali, S., Ak, S., et al. 2011, MNRAS, 417, 2230
Blondin, S., & Tonry, J. L. 2007, ApJ, 666, 1024
Boehner, P., Plewa, T., & Langer, N. 2017, MNRAS, 465, 2060
Botyánszki, J., & Kasen, D. 2017, ApJ, 845, 176
Botyánszki, J., Kasen, D., & Plewa, T. 2018, ApJL, 852, L6
Brooks, J., Bildsten, L., Marchant, P., & Paxton, B. 2015, ApJ, 807, 74
Brown, T. M., Baliber, N., Bianco, F. B., et al. 2013, PASP, 125, 1031
Cannizzaro, G., Fraser, M., Benetti, S., et al. 2016, ATel, 9703, 1
Clemens, J. C., Crain, J. A., & Anderson, R. 2004, Proc. SPIE, 5492, 331
Colgate, S. A., & McKee, C. 1969, ApJ, 157, 623
De, K., Kasliwal, M. M., Cantwell, T., et al. 2018, ApJ, 866, 72
De, K., Kasliwal, M. M., Polin, A., et al. 2019, ApJL, 873, L18
Dimitriadis, G., Pursiainen, M., Smith, M., et al. 2016, ATel, 9704, 1
Dimitriadis, G., Rojas-Bravo, C., Kilpatrick, C. D., et al. 2019, ApJL, 870, L14
Dimitriadis, G., Sullivan, M., Kerzendorf, W., et al. 2017, MNRAS, 468, 3798
Drout, M. R., Soderberg, A. M., Mazzali, P. A., et al. 2013, ApJ, 774, 58
Filippenko, A. V., Chornock, R., Swift, B., et al. 2003, IAUC, 8159, 2
Filippenko, A. V., Richmond, M. W., Branch, D., et al. 1992, AJ, 104, 1543
Fink, M., Röpke, F. K., Hillebrandt, W., et al. 2010, A&A, 514, A53
Fitzpatrick, E. L. 1999, PASP, 111, 63
Flewelling, H. A., Magnier, E. A., Chambers, K. C., et al. 2016, arXiv:1612.05243
Foley, R. J. 2015, MNRAS, 452, 2463
Foley, R. J., Challis, P. J., Chornock, R., et al. 2013, ApJ, 767, 57
Foley, R. J., Chornock, R., Filippenko, A. V., et al. 2009a, AJ, 138, 376
Foley, R. J., Jha, S. W., Pan, Y.-C., et al. 2016, MNRAS, 461, 433
Foley, R. J., Matheson, T., Blondin, S., et al. 2009b, AJ, 137, 3731
Foley, R. J., Narayan, G., Challis, P. J., et al. 2010, ApJ, 708, 1748
Foley, R. J., Papenkova, M. S., Swift, B. J., et al. 2003, PASP, 115, 1220
Foley, R. J., Scolnic, D., Rest, A., et al. 2018, MNRAS, 475, 193
Foreman-Mackey, D., Hogg, D. W., Lang, D., & Goodman, J. 2013, PASP, 125, 306
Galbany, L., Ashall, C., Hoeflich, P., et al. 2019, A&A, 630, 76
Gal-Yam, A. 2005, ATel, 655, 1
Gal-Yam, A., Xu, D., Ben-Ami, S., et al. 2011, ATel, 3631, 1
Ganeshalingam, M., Li, W., Filippenko, A. V., et al. 2012, ApJ, 751, 142
Garnavich, P. M., Bonanos, A. Z., Krisciunas, K., et al. 2004, ApJ, 613, 1120
Gonzaga, S., Hack, W., Fruchter, A., et al. 2012, The DrizzlePac Handbook (Baltimore, MD: STScI)
Graur, O., Zurek, D., Shara, M. M., et al. 2016, ApJ, 819, 31
Höflich, P., Gerardy, C. L., Fesen, R. A., & Sakai, S. 2002, ApJ, 568, 791
Horne, K. 1986, PASP, 98, 609
Howell, D. A., Sullivan, M., Perrett, K., et al. 2005, ApJ, 634, 1190
Hoyle, F., & Fowler, W. A. 1960, ApJ, 132, 565
Jacobson-Galán, W. V., Dimitriadis, G., Foley, R. J., & Kilpatrick, C. D. 2018, ApJ, 857, 88
Jacobson-Galán, W. V., Foley, R. J., Schwab, J., et al. 2019, MNRAS, 487, 2538
Kasen, D., Thomas, R. C., & Nugent, P. 2006, ApJ, 651, 366
Kasliwal, M. M., Kulkarni, S. R., Gal-Yam, A., et al. 2010, ApJL, 723, L98
Kasliwal, M. M., Kulkarni, S. R., Gal-Yam, A., et al. 2012, ApJ, 755, 161
Kromer, M., Sim, S. A., Fink, M., et al. 2010, ApJ, 719, 1067
Leibundgut, B., Kirshner, R. P., Phillips, M. M., et al. 1993, AJ, 105, 301
Li, W., Bloom, J. S., Podsiadlowski, P., et al. 2011, Natur, 480, 348
Liu, Z.-W., Kromer, M., Fink, M., et al. 2013a, ApJ, 778, 121
Liu, Z. W., Pakmor, R., Röpke, F. K., et al. 2012, A&A, 548, A2
Liu, Z.-W., Pakmor, R., Seitenzahl, I. R., et al. 2013b, ApJ, 774, 37
Livne, E., & Arnett, D. 1995, ApJ, 452, 62
Lundqvist, P., Mattila, S., Sollerman, J., et al. 2013, MNRAS, 435, 329
Lunnan, R., Kasliwal, M. M., Cao, Y., et al. 2017, ApJ, 836, 60
Lyman, J. D., Levan, A. J., Church, R. P., Davies, M. B., & Tanvir, N. R. 2014, MNRAS, 444, 2157
MacLeod, M., Goldstein, J., Ramirez-Ruiz, E., Guillochon, J., & Samsing, J. 2014, ApJ, 794, 9
Magnier, E. 2006, in The Advanced Maui Optical and Space Surveillance Technologies Conf., ed. S. Ryan (Maui, HI: AMOS), E50
Magnier, E. A., Schlafly, E., Finkbeiner, D., et al. 2013, ApJS, 205, 20
Margalit, B., & Metzger, B. D. 2016, MNRAS, 461, 1154
Marietta, E., Burrows, A., & Fryxell, B. 2000, ApJS, 128, 615
Martini, P., Elias, J., Points, S., et al. 2014, Proc. SPIE, 9147, 91470Z
Mattila, S., Lundqvist, P., Sollerman, J., et al. 2005, A&A, 443, 649
McCully, C., Jha, S. W., Foley, R. J., et al. 2014, Natur, 512, 54
Metzger, B. D. 2012, MNRAS, 419, 827
Metzger, B. D., Piro, A. L., Quataert, E., & Thompson, T. A. 2009, arXiv:0908.1127
Milisavljevic, D., Patnaude, D. J., Raymond, J. C., et al. 2017, ApJ, 846, 50
Nomoto, K. 1982a, ApJ, 253, 798
Nomoto, K. 1982b, ApJ, 257, 780
Nugent, P., Branch, D., Baron, E., et al. 1995, PhRvL, 75, 394
Nugent, P. E., Sullivan, M., Cenko, S. B., et al. 2011, Natur, 480, 344
Oke, J. B., Cohen, J. G., Carr, M., et al. 1995, PASP, 107, 375
Pan, K.-C., Ricker, P. M., & Taam, R. E. 2012, ApJ, 750, 151

Pan, Y.-C., Duarte, A. S., Foley, R. J., et al. 2016, ATel, 9705, 1
Perets, H. B., Gal-yam, A., Crockett, R. M., et al. 2011, ApJL, 728, L36
Perets, H. B., Gal-Yam, A., Mazzali, P. A., et al. 2010, Natur, 465, 322
Perlmutter, S., Aldering, G., Goldhaber, G., et al. 1999, ApJ, 517, 565
Phillips, M. M. 1993, ApJL, 413, L105
Phillips, M. M., Simon, J. D., Morrell, N., et al. 2013, ApJ, 779, 38
Polin, A., Nugent, P., & Kasen, D. 2019a, ApJ, 873, 84
Polin, A., Nugent, P., & Kasen, D. 2019b, arXiv:1910.12434
Rest, A., Stubbs, C., Becker, A. C., et al. 2005, ApJ, 634, 1103
Riess, A. G., Filippenko, A. V., Challis, P., et al. 1998, AJ, 116, 1009
Rosswog, S., Ramirez-Ruiz, E., & Hix, W. R. 2008, ApJ, 679, 1385
Sand, D. J., Graham, M. L., Botyánszki, J., et al. 2018, ApJ, 863, 24
Schechter, P. L., Mateo, M., & Saha, A. 1993, PASP, 105, 1342
Schlafly, E. F., & Finkbeiner, D. P. 2011, ApJ, 737, 103
Schlegel, D. J., Finkbeiner, D. P., & Davis, M. 1998, ApJ, 500, 525
Scolnic, D., Casertano, S., Riess, A., et al. 2015, ApJ, 815, 117
Seitenzahl, I. R., Cescutti, G., Röpke, F. K., Ruiter, A. J., & Pakmor, R. 2013,
    A&A, 559, L5
Seitenzahl, I. R., Timmes, F. X., & Magkotsios, G. 2014, ApJ, 792, 10
Sell, P. H., Arur, K., Maccarone, T. J., et al. 2018, MNRAS, 475, L111
Sell, P. H., Maccarone, T. J., Kotak, R., Knigge, C., & Sand, D. J. 2015,
    MNRAS, 450, 4198
Shappee, B. J., Stanek, K. Z., Kochanek, C. S., & Garnavich, P. M. 2017, ApJ,
    841, 48
Shen, K. J., & Bildsten, L. 2014, ApJ, 785, 61
Shen, K. J., Kasen, D., Miles, B. J., & Townsley, D. M. 2018, ApJ, 854, 52
Shen, K. J., Kasen, D., Weinberg, N. N., Bildsten, L., & Scannapieco, E. 2010,
    ApJ, 715, 767
Shen, K. J., & Moore, K. 2014, ApJ, 797, 46

Silverman, J. M., Foley, R. J., Filippenko, A. V., et al. 2012, MNRAS,
    425, 1789
Sim, S. A., Röpke, F. K., Hillebrandt, W., et al. 2010, ApJL, 714, L52
Stritzinger, M., Leibundgut, B., Walch, S., & Contardo, G. 2006, A&A,
    450, 241
Stritzinger, M. D., Valenti, S., Hoeflich, P., et al. 2015, A&A, 573, A2
Sullivan, M., Kasliwal, M. M., Nugent, P. E., et al. 2011, ApJ, 732, 118
Taubenberger, S. 2017, in Handbook of Supernovae, ed. A. Alsabti &
    P. Murdin (Berlin: Springer), 317
Thomas, R. C., Nugent, P. E., & Meza, J. C. 2011, PASP, 123, 237
Tonry, J., Denneau, L., Stalder, B., et al. 2016, ATel, 9685, 1
Tonry, J. L., Denneau, L., Heinze, A. N., et al. 2018, PASP, 130, 064505
Toonen, S., Perets, H. B., Igoshev, A. P., Michaely, E., & Zenati, Y. 2018,
    A&A, 619, A53
Townsley, D. M., Miles, B. J., Shen, K. J., & Kasen, D. 2019, ApJ, 878, 38
Valenti, S., Yuan, F., Taubenberger, S., et al. 2014, MNRAS, 437, 1519
van den Bergh, S., Li, W., & Filippenko, A. V. 2005, PASP, 117, 773
Wade, R. A., & Horne, K. 1988, ApJ, 324, 411
Waldman, R., Sauer, D., Livne, E., et al. 2011, ApJ, 738, 21
Waters, C. Z., Magnier, E. A., Price, P. A., et al. 2016, arXiv:1612.05245
Woosley, S. E., & Kasen, D. 2011, ApJ, 734, 38
Woosley, S. E., Pinto, P. A., & Hartmann, D. 1989, ApJ, 346, 395
Woosley, S. E., Taam, R. E., & Weaver, T. A. 1986, ApJ, 301, 601
Woosley, S. E., & Weaver, T. A. 1994, ApJ, 423, 371
Yaron, O., & Gal-Yam, A. 2012, PASP, 124, 668
Zenati, Y., Perets, H. B., & Toonen, S. 2019a, MNRAS, 486, 1805
Zenati, Y., Toonen, S., & Perets, H. B. 2019b, MNRAS, 482, 1135
Zhang, K., Wang, X., Zhang, J., et al. 2016, ApJ, 820, 67
Zingale, M., Nonaka, A., Almgren, A. S., et al. 2013, ApJ, 764, 97